Quantized transport and steady states of Floquet topological insulators

Iliya Esin,[1] Mark S. Rudner,[2] Gil Refael,[3] and Netanel H. Lindner[1]
[1]*Physics Department, Technion, 320003 Haifa, Israel*
[2]*Center for Quantum Devices and Niels Bohr International Academy, Niels Bohr Institute, University of Copenhagen, 2100 Copenhagen, Denmark*
[3]*Institute for Quantum Information and Matter, Caltech, Pasadena, California 91125, USA*

(Received 11 January 2018; published 6 June 2018)

Robust electronic edge or surface modes play key roles in the fascinating quantized responses exhibited by topological materials. Even in trivial materials, topological bands and edge states can be induced *dynamically* by a time-periodic drive. Such Floquet topological insulators (FTIs) inherently exist out of equilibrium; the extent to which they can host quantized transport, which depends on the steady-state population of their dynamically induced edge states, remains a crucial question. In this work, we obtain the steady states of two-dimensional FTIs in the presence of the natural dissipation mechanisms present in solid state systems. We give conditions under which the steady-state distribution resembles that of a topological insulator in the Floquet basis. In this state, the distribution in the Floquet edge modes exhibits a sharp feature akin to a Fermi level, while the bulk hosts a small density of excitations. We determine the regimes where topological edge-state transport persists and can be observed in FTIs.

DOI: 10.1103/PhysRevB.97.245401

I. INTRODUCTION

Periodic driving has recently attracted interest as a promising tool for exploring new phases of quantum matter [1–23]. Beyond accessing phases resembling those accessible in equilibrium, "Floquet engineering" also gives access to anomalous, intrinsically nonequilibrium dynamical phases [18–29]. Topological bands of periodically driven systems have been demonstrated in experiments in solid state [30,31], cold atoms [32–36], and optical systems [37,38].

One of the most exciting prospects of Floquet engineering is the possibility to induce robust quantized responses in topologically trivial materials. In equilibrium, the combination of nontrivial band topology and thermodynamics gives rise to quantized transport with metrological precision at low temperatures. When nontrivial band topology is induced dynamically, the system is out of equilibrium [39–44]; thus we must find new mechanisms for stabilizing quantized transport. The limits on quantization in the nonequilibrium setting are set by the dynamics of the system coupled to its environment, and the resulting steady states that are formed. In particular, when the system is longer than the inelastic mean free path (MFP), transport depends crucially on the interplay between the coupling to the system's leads and to its intrinsic baths. Our goal is to determine how to control the fidelity of quantized transport in this setting.

In this work, we consider a two-dimensional (2D) Floquet topological insulator which features chiral Floquet edge modes in a finite geometry (see Fig. 1). In such a driven electronic system, the natural intrinsic baths to consider are the phonons of the crystal lattice and the photons of the ambient electromagnetic environment. The role of acoustic phonons is mainly to relax momentum and (quasi)energy, while photon emission associated with particle-hole recombination acts as a primary heating source in the Floquet band picture (similar considerations were applied to one-dimensional systems in

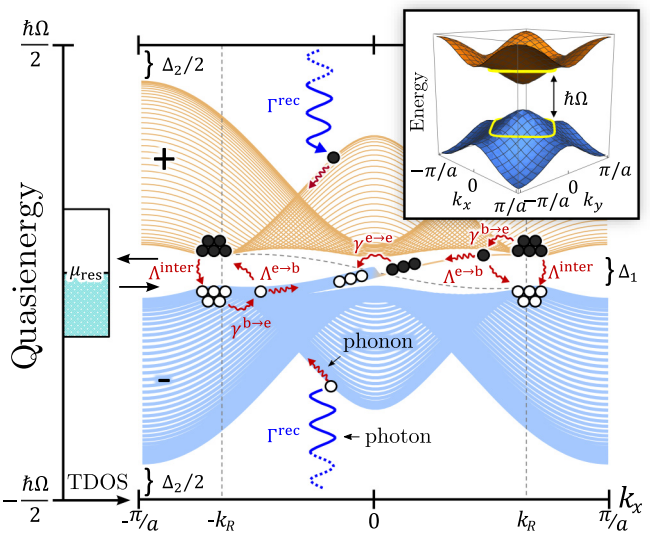

FIG. 1. Quasienergy spectrum of a 2D Floquet topological insulator in a cylindrical geometry. Wavy arrows illustrate processes due to electron-boson interactions, captured phenomenologically in Eq. (5). Excitations from the lower to the upper bulk Floquet band are mediated by radiative recombination (with rate Γ^{rec}). Relaxation to the lower Floquet band is mediated by phonons (Λ^{inter}). Phonons also mediate transitions between the bulk and the edge ($\gamma^{\mathrm{b}\to\mathrm{e}}$ and $\Lambda^{\mathrm{e}\to\mathrm{b}}$) and within the edge ($\gamma^{\mathrm{e}\to\mathrm{e}}$). These processes yield an insulatorlike steady-state filling of the Floquet bands, with additional electron and hole excitations (filled and empty circles, respectively). The system is coupled to an energy-filtered Fermi reservoir with a narrow effective bandwidth (left). Inset: The nondriven bulk spectrum of the system. The yellow loops depict the resonance condition of the periodic drive.

Ref. [43]). Due to the edges of the system, the steady state is inhomogeneous, and therefore we analyze the system using a Floquet-Boltzmann approach [45]. To deduce the transport properties of the system, we also consider the effects of a coupling to an external Fermi reservoir (i.e., a lead).

Below we show that the steady state, characterized by the populations of Floquet-Bloch states, resembles that of a topological insulator, with an additional nonequilibrium Fermi sea of electrons and holes in the bulk. The chiral Floquet edge states are populated according to a smooth distribution with a well defined Fermi level. In the presence of coupling to an energy-filtered Fermi reservoir, whose chemical potential lies in the Floquet band gap [43], we find that (1) the bulk excitation density is insensitive to variations of the reservoir chemical potential and (2) the Fermi level of the edge states is pinned to the chemical potential of the reservoir. Using these results, we show that the fidelity of quantized transport improves exponentially with the ratio of recombination to electron-phonon scattering rates.

II. MODEL OF THE FTI

We now introduce the model for the driven system. We consider a two-band 2D model, described in the absence of driving by the Hamiltonian

$$\hat{\mathcal{H}}_0 = \sum_{\boldsymbol{k}} \hat{c}^\dagger_{\boldsymbol{k}\nu} (\mathbf{d}(\boldsymbol{k}) \cdot \boldsymbol{\sigma})_{\nu\nu'} \hat{c}_{\boldsymbol{k}\nu'}, \tag{1}$$

where $\boldsymbol{\sigma} = (\sigma^x, \sigma^y, \sigma^z)$ is the vector of Pauli matrices, and $\hat{c}^\dagger_{\boldsymbol{k}\nu}$ creates an electron with quasimomentum $\boldsymbol{k}$ and pseudospin $\nu = \{\uparrow, \downarrow\}$. We take $\mathbf{d}(\boldsymbol{k}) = (A \sin(ak_x), A \sin(ak_y), M - 4B + 2B\cos(ak_x) + 2B\cos(ak_y))$, such that Eq. (1) describes half the degrees of freedom in the BHZ model for time-reversal invariant semiconductor quantum wells [46–48]. Here A, B, and M are material-dependent parameters, and a is the lattice constant of the crystal. We assume a trivial semiconductor (with noninverted band structure), with $M > 0$ and $B < 0$.

The semiconductor is periodically driven by an external field with an above-gap frequency Ω. For simplicity, we consider a uniform driving field of amplitude V_0 that couples to electrons through σ^z,[1] modeled by the time-dependent Hamiltonian

$$\hat{\mathcal{H}}_V(t) = \frac{1}{2} V_0 \cos(\Omega t) \sum_{\boldsymbol{k}} \hat{c}^\dagger_{\boldsymbol{k}\nu} \sigma^z_{\nu\nu'} \hat{c}_{\boldsymbol{k}\nu'}. \tag{2}$$

The qualitative results we present in the paper do not depend on the details of the driving field, but only on the topological features of the band structure (see discussion below).

Below we work in the basis of Floquet-Bloch eigenstates of the time-periodic single particle Hamiltonian $\hat{\mathcal{H}}_0 + \hat{\mathcal{H}}_V(t) = \sum_{\boldsymbol{k}} \hat{c}^\dagger_{\boldsymbol{k}\nu} [H(t)]_{\boldsymbol{k},\nu\nu'} \hat{c}_{\boldsymbol{k}\nu'}$. The Floquet eigenstates satisfy $(i\hbar \frac{\partial}{\partial t} - H(t))|\psi(t)\rangle = 0$, with $|\psi(t)\rangle = e^{-i\varepsilon t/\hbar}|\phi(t)\rangle$. Here, $|\phi(t)\rangle = |\phi(t+T)\rangle$ is periodic with period $T = 2\pi/\Omega$, and ε is the quasienergy. Throughout, we use the convention $-\hbar\Omega/2 \leqslant \varepsilon < \hbar\Omega/2$.

[1] More realistic time-dependent electromagnetic fields can be incorporated in this model, see Ref. [7].

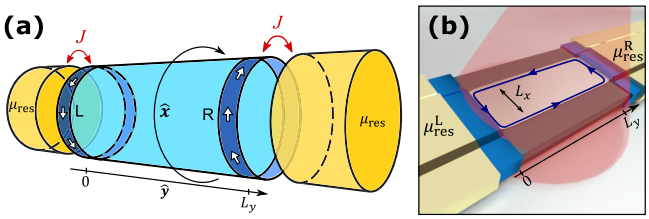

FIG. 2. (a) Schematic drawing of the system coupled to leads in the cylinder geometry. Dark blue rings indicate the right (R) and left (L) edge states. The energy filtered leads are set to have equal chemical potentials, $\mu_{\rm res}$, coupling strength to the system J, and density of states. (b) Two-terminal transport geometry. Contacts (yellow) are connected to a periodically driven semiconductor (white) through an energy filter (blue).

The driving field yields resonant transitions between the valence and conduction bands along a closed curve in momentum space, see Fig. 1 (inset). A gap of magnitude $\Delta_1 \propto |V_0|$ opens at quasienergy $\varepsilon = 0$ (corresponding to energy $\hbar\Omega/2$ of the static system), yielding two separate quasienergy bands. The driving field leads to an effective band inversion of the Floquet bands with respect to the original nondriven band structure. An important consequence of this band inversion is the appearance of chiral edge states in the gap at $\varepsilon = 0$ for a system in a finite geometry with edges [7]. We restrict $\hbar\Omega > |M - 8B|$, such that there is only a single-photon resonance.[2]

We label the bulk Floquet states by the quasimomentum $\boldsymbol{k}$ and a Floquet band index $\alpha = \pm$ (distinct from the band index of the nondriven system): $|\psi_{\boldsymbol{k}\alpha}(t)\rangle = e^{-i\varepsilon_\alpha(\boldsymbol{k})t/\hbar} \sum_m e^{im\Omega t} |\phi^m_{\boldsymbol{k}\alpha}\rangle$ [49,50]. We refer to the Floquet bands with quasienergies $0 < \varepsilon < \hbar\Omega/2$ and $-\hbar\Omega/2 < \varepsilon < 0$ as the upper (+) and lower (−) Floquet bands, respectively, see Fig. 1.

In the following, we will consider a system with periodic boundary conditions in the x direction, and open boundary conditions in the y direction. As seen in Fig. 1, in this geometry, the edge states exist for quasimomentum k_x in the interval $-k_R \lesssim k_x \lesssim k_R$, where k_R is the maximal value of k_x for which the driving field is resonant. We denote the Floquet edge states as $|\chi_{k_x\beta}(t)\rangle$, where the label β corresponds to the left (L) and right (R) edges (at $y = 0$ and $y = L_y$), for which $\partial\varepsilon/\partial k_x$ is negative and positive, respectively, see Fig. 2(a).

III. COUPLING TO A BOSONIC HEAT BATH

The open, driven system evolves to a steady state, governed by its coupling to one or more heat baths (taken to be at zero temperature). We first focus on the bosonic bath, and consider the roles of acoustic phonons and photons (associated with radiative recombination). Using the label $\lambda = \ell, s$ to denote the photon (light) and acoustic phonon (sound) modes, we describe

[2] The Floquet gaps resulting form higher order resonances, if present, would be suppressed by powers of $|V_0|/\hbar\Omega$. Therefore their primary role would be to add additional heating channels which would only affect the quantitative features of our results.

the dynamics of each mode by the Hamiltonian

$$\hat{\mathcal{H}}_\lambda = \sum_{\boldsymbol{q}} \hbar v_\lambda |\boldsymbol{q}| \left(\hat{b}^\dagger_{\lambda,\boldsymbol{q}} \hat{b}_{\lambda,\boldsymbol{q}} + \frac{1}{2} \right). \tag{3}$$

Here, $\hat{b}^\dagger_{\lambda,\boldsymbol{q}}$ are creation operators of λ-bosons. The velocity v_λ is taken to be constant and isotropic for each mode. While the electronic degrees of freedom are confined to a 2D plane, we take the bosonic bath modes to live in three dimensions; for simplicity we consider a single polarization mode for each boson type. For the (finite bandwidth) acoustic phonon bath, we take a linear dispersion up to a Debye frequency ω_D.[3]

Inspired by the physics of semiconductor quantum wells, we assume that emission of a photon is accompanied by a pseudospin flip (corresponding to a change of one unit of electronic angular momentum). Furthermore, we take the interaction with acoustic phonons to conserve the pseudospin index, as acoustic phonons have suppressed matrix elements between different atomic orbitals. The Hamiltonian describing local interactions between electrons and λ bosons thus reads

$$\hat{\mathcal{H}}_{e-\lambda} = \sum_{\boldsymbol{r}} \hat{c}^\dagger_{\boldsymbol{r}\nu} [\eta^\dagger_{\lambda,\nu\nu'} \hat{b}^\dagger_{\lambda,\boldsymbol{r}} + \eta_{\lambda,\nu\nu'} \hat{b}_{\lambda,\boldsymbol{r}}] \hat{c}_{\boldsymbol{r}\nu'}, \tag{4}$$

where $\eta_s = g_s \mathbb{1}$ for electron-phonon coupling, and $\eta_\ell = g_\ell \sigma^+$ for electron-photon coupling. The quantities g_ℓ and g_s denote the associated coupling strengths. In Eq. (4), the coordinate $\boldsymbol{r}$ is confined to the 2D plane.

In closing this section defining the model, we note that the full Hamiltonian possesses particle-hole and inversion symmetry at all t. The system's Floquet spectrum and the kinetic equations derived below exhibit corresponding symmetries. However, our qualitative conclusions do not depend on these symmetries.

IV. PHENOMENOLOGICAL MODEL FOR THE STEADY STATE

Before diving into the full kinetic equation, we first characterize the steady states using a simplified phenomenological model, which takes into account the most significant contributions to the population kinetics in the system (see Fig. 1). In the following discussion, we restrict our attention to a half-filled system.

Generically, the population kinetics in a driven system differs from that of a system in thermal equilibrium, due to scattering processes in which the total quasienergies of the incoming and outgoing modes differ by integer multiples of $\hbar\Omega$. As a starting point, we first consider a system in which the sums of quasienergies of the incoming modes and outgoing modes are strictly equal in all scattering processes (which requires the system-bath coupling to obey special conditions [51–55]). In this situation, the steady state of the driven system is simply given by a Fermi-Dirac distribution in terms of the Floquet bands, with the ordering of quasienergies (i.e., choice of Floquet-Brillouin zone) as used in Fig. 1. The temperature of the distribution is that of the phonon bath. For a half-filled system, we obtain an ideal FTI: when the bath is at zero temperature, the lower (upper) Floquet band is filled (empty), and the edge state is filled up to the Fermi level at $\varepsilon = 0$ (corresponding to $k_x = 0$).

Our goal is to obtain the steady state of the system in the presence of *all* scattering processes, including those where the total quasienergy changes by a multiple of $\hbar\Omega$. These "Floquet-umklapp" processes, which occur even when the bath is at zero temperature, create excitations from the lower to the upper Floquet band. Thereby, they act as a source of "quantum heating" in the Floquet basis [56,57]. We characterize the steady state in the bulk by the density of excited electrons in the "upper" (+) bulk Floquet band, $n_\mathrm{b} = \int \frac{d^2\boldsymbol{k}}{(2\pi)^2} \langle \hat{\psi}^\dagger_{\boldsymbol{k}+}(t) \hat{\psi}_{\boldsymbol{k}+}(t) \rangle$. At each edge, the steady state is characterized by the density of excited particles above the Fermi level of the ideal FTI ($\varepsilon = 0$). For the right edge, this density is given by $n_\mathrm{e} = \int_0^{k_R} \frac{dk_x}{2\pi} \langle \hat{\chi}^\dagger_{k_x R}(t) \hat{\chi}_{k_x R}(t) \rangle$. The operators $\hat{\psi}^\dagger_{\boldsymbol{k}\alpha}(t)$ and $\hat{\chi}^\dagger_{k_x\beta}(t)$ create electrons in the bulk and edge Floquet states $|\psi_{\boldsymbol{k}\alpha}(t)\rangle$ and $|\chi_{k_x\beta}(t)\rangle$, respectively.[4] The distributions of electrons in states with $\varepsilon > 0$ and of holes in states with $\varepsilon < 0$ are related by particle hole symmetry (see below). Additionally, the distributions in the right and left edge states are related by inversion symmetry.

For a semiconductor with a sufficiently large band gap, such that $M \gg \hbar\omega_\mathrm{D}$, Floquet-umklapp processes resulting from phonon scattering are suppressed as $[V_0/(\hbar\Omega)]^4$ [43]. For simplicity, in our analysis, we will assume that all Floquet umklapp process are due to radiative recombination. Since this process involves emission of a photon, it predominately contributes when the characters of the initial and final states correspond to the conduction and valence bands of the undriven system, respectively (recall that the electron-photon coupling is off-diagonal in pseudospin). Close to the ideal FTI steady state, $\boldsymbol{k}$ modes in the lower Floquet band with momenta inside the resonance curve are filled, and have a conduction band character, while those of the upper band are empty and have valence band character. Radiative recombination between these states leads to a source term for particles in the upper Floquet band, $\dot{n}_\mathrm{b} = \Gamma^\mathrm{rec}$ (see Fig. 1), with rate Γ^rec approximately independent of the excitation density for small deviations from the ideal FTI state.

Once excited to the upper Floquet band, electrons quickly relax to the band minima due to scattering by phonons. Near the Floquet band minima (around the resonance curve), the Floquet states are hybridized superpositions of valence and conduction band states. This hybridization allows phonons to scatter electrons from these minima to empty states near the maxima of the lower Floquet band. Consider the rate of such phonon-assisted "recombination" of Floquet-band carriers. During such a process, an electron in the upper band must find a hole in the lower band. The resulting rate is thus proportional to the density of electrons times that of the holes (which are equal at half-filling): $\dot{n}_\mathrm{b} \approx -\Lambda^\mathrm{inter} n_\mathrm{b}^2$.

[3] In this work, we use simple models for the acoustic phonons and the electromagnetic environment, and their couplings to the system. More detailed modeling of these baths would not qualitatively change our results.

[4] The operators $\hat{\psi}^\dagger_{\boldsymbol{k}\alpha}(t)$ and $\hat{\chi}^\dagger_{k_x\beta}(t)$ obey the anticommutation relations $\{\hat{\psi}^\dagger_{\boldsymbol{k}\alpha}(t), \hat{\psi}_{\boldsymbol{k}'\alpha'}(t)\} = \delta_{\boldsymbol{k}\boldsymbol{k}'}\delta_{\alpha\alpha'}$ and $\{\hat{\chi}^\dagger_{k_x\beta}(t), \hat{\chi}_{k_x'\beta'}(t)\} = \delta_{k_x k_x'}\delta_{\beta\beta'}$.

Next, we account for processes which scatter particles between bulk and edge states. Such bulk-edge scattering processes are predominantly phonon-assisted (the rates for photon-assisted bulk-edge scattering are suppressed by a small density of states). Assuming a small population of excited electrons (with $\varepsilon > 0$) on the edge, $n_e \ll 1/a$, bulk-to-edge processes predominantly take excited electrons in the upper Floquet band to the nearly empty k-space region of the edge states (with $k_x > 0$, for the right edge). In contrast, edge-to-bulk processes require that the scattered edge electron finds an empty bulk state (i.e., a hole) in the lower Floquet band (see Fig. 1). The corresponding rate is thus proportional to both the densities of excitations on the edge and in the bulk. We therefore estimate the contribution of bulk-edge processes to $\dot{n}_e$ as $\dot{n}_e = \gamma^{b\to e} n_b - \Lambda^{e\to b} n_b n_e$. The parameters $\gamma^{b\to e}$ and $\Lambda^{e\to b}$ encode the rates of bulk-to-edge and edge-to-bulk scattering processes, respectively.

Last, we account for phonon-assisted scattering of particles within the edge. At low phonon temperatures, such processes predominately decrease the quasienergy of the electrons, and thus tend to decrease the density of excited particles on the edge. The requirement that an excited edge-electron finds an edge-hole gives $\dot{n}_e = \gamma^{e\to e} n_e^2$.

Summing up the processes above, we arrive at the rate equations for the bulk and edge excitation densities:

$$\dot{n}_b = \Gamma^{rec} - \Lambda^{inter} n_b^2 - \frac{2}{L_y}(\gamma^{b\to e} n_b - \Lambda^{e\to b} n_b n_e), \quad (5a)$$

$$\dot{n}_e = \gamma^{b\to e} n_b - \Lambda^{e\to b} n_b n_e - \gamma^{e\to e} n_e^2. \quad (5b)$$

The steady-state solution for the above equations is obtained for $\dot{n}_b = \dot{n}_e = 0$.

In the thermodynamic limit, the rate parameters in Eq. (5) become independent of system size (see Appendix A). Note that in Eq. (5a), the source term for the 2D density n_b due to coupling to the 1D edge is multiplied by a factor of $1/L_y$. Thus, for $L_y \to \infty$, Eq. (5a) yields a bulk excitation density n_b which is independent of n_e, and scales as

$$n_b \approx \kappa^{\frac{1}{2}}, \quad \kappa = \Gamma^{rec}/\Lambda^{inter}. \quad (6)$$

As expected, the bulk excitation density is unaffected by the presence of the edge. The dimensionless parameter κa^4 captures the competition between "heating" (Floquet-umklapp) and "cooling" processes in the bulk.

The rates controlling the excitation density on the edge in Eq. (5b) are predominantly due to phonon-assisted scattering. Therefore their ratios do not scale with κ. For sufficiently small κ, we reach $\frac{\gamma^{e\to e}\gamma^{b\to e}}{(\Lambda^{e\to b})^2} \gg n_b$. In this limit, the second term in Eq. (5b) can be omitted and we find for the steady state:

$$n_e \approx (\gamma^{b\to e}/\gamma^{e\to e})^{\frac{1}{2}} \kappa^{\frac{1}{4}}, \quad (7)$$

where the ratio $\gamma^{b\to e}/\gamma^{e\to e}$ is independent of κ.

The bulk excitation density n_b estimated in Eq. (6) represents a spatial average over the full system. In a more detailed picture, we expect the excitation density to be inhomogeneous, deviating from the bulk value estimated in Eq. (6) near the edges. We investigate the spatial dependence of n_b below.

V. MICROSCOPIC ANALYSIS OF THE STEADY STATE

We now turn to a more microscopic treatment, and characterize the steady state using a Floquet-Boltzmann equation approach. We focus on the regime where the MFP is larger than the characteristic wavelength of electrons. We characterize the steady state in the bulk in terms of a phase space distribution function $f^b_{k\alpha}(\boldsymbol{r};t)$. Due to the translational invariance of the cylinder, we assume that the phase space distribution is independent of x. Therefore we define

$$f^b_{k\alpha}(y;t) = \frac{L_y}{\pi}\int dk'_y e^{2ik'_y y}\langle \hat{\psi}^\dagger_{k+k'_y\hat{y}\alpha}(t)\hat{\psi}_{k-k'_y\hat{y}\alpha}(t)\rangle. \quad (8)$$

Note that $\int \frac{d^2k}{(2\pi)^2} f^b_{k\alpha}(y;t)$ gives the density of electrons in band α at position y (for any x), at time t.[5] A dependence on y is expected due to the edges at $y = 0, L_y$. The distributions within the one-dimensional edge states are defined as $f^e_{k_x\beta}(t) = \langle \hat{\chi}^\dagger_{k_x\beta}(t)\hat{\chi}_{k_x\beta}(t)\rangle$.

Next, we study the steady-state behavior of $f^b_{k\alpha}(y)$. The physics on length scales larger than the MFP is described by the Floquet-Boltzmann equation [45],

$$\partial_t f^b_{k\alpha} + v_{y,\alpha}(k)\partial_y f^b_{k\alpha} = \mathcal{I}^{bb}_{k\alpha} + \mathcal{I}^{bR}_{k\alpha} + \mathcal{I}^{bL}_{k\alpha}. \quad (9)$$

Here, $v_{y,\alpha}(k) = \hbar^{-1}\partial_{k_y}\varepsilon_\alpha(k)$ is the Floquet band group velocity in the y direction, and the collision integrals $\mathcal{I}^{bb}_{k\alpha}$, $\mathcal{I}^{bR}_{k\alpha}$, and $\mathcal{I}^{bL}_{k\alpha}$ describe bulk-bulk, bulk-right-edge and bulk-left-edge scattering processes, respectively. For brevity, in Eq. (9), we used $f^b_{k\alpha} \equiv f^b_{k\alpha}(y;t)$; likewise, we suppressed the dependence of the collision integrals on y and t. The Boltzmann equation for the edges has a similar structure, namely, $\partial_t f^e_{k_x\beta} = \mathcal{I}^{ee}_{k_x\beta} + \mathcal{I}^{eb}_{k_x\beta}$.

In explicit form, the collision integral for bulk-to-bulk scattering processes is given by

$$\mathcal{I}^{bb}_{k\alpha} = \sum_{k'\alpha'}\left[W^{k\alpha}_{k'\alpha'} f^b_{k'\alpha'}(1 - f^b_{k\alpha}) - W^{k'\alpha'}_{k\alpha} f^b_{k\alpha}(1 - f^b_{k'\alpha'})\right], \quad (10)$$

where $W^{k\alpha}_{k'\alpha'}$ is the total scattering rate from (k,α) to (k',α'). The rates $W^{k\alpha}_{k'\alpha'}$ in Eq. (10) are y-independent, and therefore any y dependence of $\mathcal{I}^{bb}_{k\alpha}$ arises through the distributions $f^b_{k\alpha}(y;t)$. In contrast, for the bulk-edge collision integrals $\mathcal{I}^{bR}_{k\alpha}$ and $\mathcal{I}^{bL}_{k\alpha}$, the corresponding rates themselves are only significant for values of y near the edges, due to the spatial profile of the edge states. The full expressions for all the collision integrals can be found in Appendix A.

The rate $W^{k'\alpha'}_{k\alpha}$ in Eq. (10) can be written as a sum of phonon (s) and photon (ℓ) assisted scattering rates, $W^{k'\alpha'}_{k\alpha} = W^{k'\alpha'}_{\ell,k\alpha} + W^{k'\alpha'}_{s,k\alpha}$, given by

$$W^{k'\alpha'}_{\lambda,k\alpha} = \frac{2\pi}{\hbar}\sum_n \left|\sum_m \langle \phi^m_{k\alpha}|\eta_\lambda|\phi^{m-n}_{k'\alpha'}\rangle\right|^2 \times \rho_\lambda(\varepsilon_\alpha(k) - \varepsilon_{\alpha'}(k') + n\hbar\Omega, k - k'). \quad (11)$$

[5] Off-diagonal correlations between states separated by a large gap (with respect to the scattering rate) are suppressed [43,77].

The DOS of λ bosons is given by $\rho_\lambda(\varepsilon,\boldsymbol{q}) = \frac{a^2}{L_x L_y}\frac{a\varepsilon\Theta(\varepsilon-\hbar v_\lambda|\boldsymbol{q}|)}{\pi\hbar v_\lambda\sqrt{\varepsilon^2-\hbar^2 v_\lambda^2|\boldsymbol{q}|^2}}$, where (as above) $\lambda = \{s,\ell\}$. For relatively low-energy emission processes [e.g., relaxation across the Floquet gap, contributing to Λ^{inter} in Eq. (5b)], the photon DOS is suppressed relative to the phonon DOS by v_s/v_ℓ and phonon-emission dominates. For high energy transfers, the DOS of phonons vanishes when ε is above the Debye energy, $\hbar\omega_D$. In this work, we fix ω_D within the range $\Delta_1 < \hbar\omega_D < \Delta_2$, ensuring Floquet-umklapp processes induced by phonon scattering are fully suppressed. Here, Δ_1 and Δ_2 are the gaps centered at $\varepsilon = 0$ and $\varepsilon = \hbar\Omega/2$, respectively, see Fig. 1.

Within this formalism, we can estimate the phenomenological rates in the effective model, Eq. (5), using microscopic parameters (for full details see Appendix A). We denote by $\mathcal{W}^{\text{rec}}_{\boldsymbol{k}} = (\frac{L_x L_y}{4\pi}\frac{\Omega^2}{v_\ell^2})W^{\boldsymbol{k}+}_{\ell,\boldsymbol{k}-}$ the recombination rate for particles initially in the lower Floquet band. This rate is significant within the resonance curve, where the Floquet bands are inverted and the characters of the initial and the final states correspond to the conduction and valence bands of the nondriven system, respectively. Thus the source term for the bulk excitation density is $\Gamma^{\text{rec}} \approx \int \frac{d^2\boldsymbol{k}}{(2\pi)^2}\mathcal{W}^{\text{rec}}_{\boldsymbol{k}} \equiv \frac{A_{\mathcal{R}}}{(2\pi)^2}\overline{\mathcal{W}}^{\text{rec}}$, where $A_{\mathcal{R}}$ is the momentum-space area inside the resonance curve. We estimate the parameter Λ^{inter} characterizing phonon-assisted relaxation between Floquet bands as $\Lambda^{\text{inter}} \approx L_x L_y \overline{\mathcal{W}}^{\text{inter}}$, where $\overline{\mathcal{W}}^{\text{inter}} = W^{\boldsymbol{k}_R-}_{s,\boldsymbol{k}_R+}$ is an average relaxation rate of a particle in the active region around the minimum of the upper Floquet band. With these definitions, we obtain an approximate expression for κ in Eq. (6): $\kappa \approx \frac{A_{\mathcal{R}}\Omega^2 v_s g_\ell^2}{8\pi^3 v_\ell^3 g_s^2}$. The parameters $\gamma^{\text{b}\to\text{e}}$, $\Lambda^{\text{e}\to\text{b}}$, and $\gamma^{\text{e}\to\text{e}}$ can be estimated using the bulk-to-edge and edge-to-edge scattering rates in the same manner.

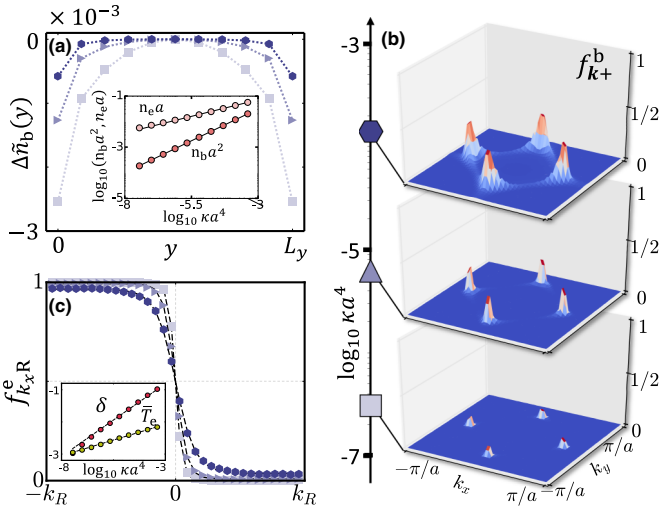

FIG. 3. Steady state of electrons in a half-filled system. The simulation was performed using a discretization with a 50×50 grid in momentum space, and 11 strips in the y direction (of width comparable to the healing length ξ, see text, and Appendix C). (a) Change in spatial dependence of the excitation density in the bulk bands, normalized by the excitation density deep in the bulk, $\Delta\tilde{n}_{\text{b}}(y) = (n_{\text{b}}(y) - n^0_{\text{b}})/n^0_{\text{b}}$, with $n^0_{\text{b}} = n_{\text{b}}(L_y/2)$, for three values of κ. The color code indicating the values of κ appears to the right. (Inset) Scaling of the bulk ($n^0_{\text{b}}a^2$) and edge ($n_{\text{e}}a$) excitation densities with κa^4, and the fits $n_{\text{e}}a \sim (\kappa a^4)^{0.26}$, $n^0_{\text{b}}a^4 \sim (\kappa a^4)^{0.5}$ (black lines). (b) Distribution of particles in the upper Floquet band ($f^{\text{b}}_{\boldsymbol{k}+}$) far away from the edges, for different values of κ. (c) Carrier distribution of the right edge ($f^{\text{e}}_{k_x\text{R}}$) for the same values of κ as in (a) and (b), and the nonlinear least-squares fit to the quasi Fermi-Dirac distribution (dashed lines). (Inset) Effective temperature of the edge, $\bar{T}_{\text{e}} = k_{\text{B}}T_{\text{e}}/\hbar\Omega$, and the δ parameter of the quasi-Fermi-Dirac functionversus κa^4. Dashed lines represent the fits $\bar{T}_{\text{e}} \sim (\kappa a^4)^{0.19}$, and $\delta \sim (\kappa a^4)^{0.45}$.

VI. NUMERICAL SIMULATIONS

We now numerically solve Eq. (9) in the steady state, taking $\dot{f}_{\boldsymbol{k}\alpha} = 0$. We consider the system at half-filling. Figure 3(a) shows the spatial dependence of the bulk excitation density, $n_{\text{b}}(y) = \int d^2\boldsymbol{k}\, f_{\boldsymbol{k}+}(y)$, for three values of κ. Away from the edges, the density reaches a position-independent "bulk" value, n^0_{b}. The dependence of n^0_{b} on κa^4 is shown in the inset of Fig. 3(a), and agrees well with our estimate in Eq. (6).

The spatial dependence of $n_{\text{b}}(y)$ can be accounted for by generalizing Eq. (5a) to a reaction-diffusion equation [43] (see Appendix B). From this picture we extract the "healing length" ξ over which the excitation density relaxes to the bulk value n^0_{b}: $\xi \approx \sqrt{Dn^0_{\text{b}}/(2\Gamma_{\text{rec}})}$, where D is the diffusion constant. Taking $D \approx \bar{v}^2\tau$, where $\bar{v}$ is a typical velocity of the excited carriers in the steady state and τ is the scattering time (due to phonons), we find good agreement with the length scales exhibited by our numerical results (see Appendix C).

Figure 3(b) shows steady-state distributions of the bulk far away from the edges, for three different values of κa^4. The steady-state distribution of the upper band is well described by a Floquet-Fermi-Dirac distribution (a Fermi-Dirac distribution in terms of the quasienergy spectrum), with an effective temperature and chemical potential obtained as fitting parameters. The distribution of the lower band is related by particle-hole symmetry, $f^{\text{b}}_{\boldsymbol{k},-} = 1 - f^{\text{b}}_{-\boldsymbol{k},+}$. The chemical potential describing the distribution in the upper band does not lie in the middle of the gap. Therefore, to describe the distribution of the system, we must use two separate Fermi-Dirac distributions, with distinct chemical potentials, for the upper and lower Floquet bands (for a full analysis of the fit to the Floquet-Fermi-Dirac distribution, see Appendix D). Analogous distributions were found for a 1D system in Ref. [43]. In the absence of photon-assisted recombination (i.e., when $\kappa a^4 \to 0$), the steady state converges to a global zero-temperature Gibbs state over the Floquet spectrum [51–53].

The steady-state distribution of the particles along the right edge is shown in Fig. 3(c). The distribution of the left edge is related by inversion symmetry, $f^{\text{e}}_{k_x\text{L}} = f^{\text{e}}_{-k_x\text{R}}$. We observe that the excitations in the edge states predominantly accumulate near $k_x \sim 0$. The shape of the distribution is approximated to a good accuracy by a "quasi-Fermi-Dirac distribution," defined as $f_{\text{QFD}}(\varepsilon) = (1-\delta)f_{\text{FD}}(\varepsilon,T_{\text{e}}) + \frac{1}{2}\delta$. Here, $f_{\text{FD}}(\varepsilon,T_{\text{e}})$ is the conventional Fermi function, which we scale by a contrast factor ($0 < \delta < 1$) to create f_{QFD}. The form of the function f_{QFD} dictates that the effective temperature T_{e} is approximately proportional to the excitation density on the edge, n_{e}. The δ parameter describes a small density of particles (holes), uniformly spread along the $k_x > 0$ ($k_x < 0$) part of the edge

mode. The electron and hole "pockets" at the extrema of the bulk Floquet bands provide the source for this excess density. Thus we expect δ to exhibit a similar scaling with κ as the density of bulk electrons $n_{\rm b}$. The dependence of $n_{\rm e}a$, and of the fitted parameters $T_{\rm e}$ and δ on κa^4 are shown in the insets of Figs. 3(a) and 3(c). The results of our simulations are in a good agreement with Eqs. (6) and (7) and the scaling arguments above.

VII. COUPLING TO A FERMI RESERVOIR

How are the topological properties of FTIs manifested in transport measurements? To study this question, we couple the system to Fermi reservoirs at the two edges, $y = 0$ and $y = L_y$, see Fig. 2(a). The Hamiltonian describing the right reservoir and its coupling to the system reads

$$\hat{\mathcal{H}}^{\rm R}_{\rm res} = \sum_{lp}(J_{lp}\hat{d}^\dagger_l\hat{c}_p + \text{H.c.}) + \sum_l(\mathcal{E}_l - \mu_{\rm res})\hat{d}^\dagger_l\hat{d}_l. \quad (12)$$

Here we have introduced a superindex p labeling system operators, Fourier transformed with respect to x: $p = \{k_x, y, \nu\}$. Furthermore, $\hat{d}^\dagger_l$ is the creation operator for an electron in mode $|l\rangle$ of the right reservoir. For simplicity, we choose a system-lead coupling that does not introduce a preferred direction in pseudospin space. This is accomplished by taking two degenerate sets of modes, labeled by $l = \{k_x, \mathcal{E}_l, \nu\}$, where $\mathcal{E}_l$ is the mode's energy (which is independent of $\nu = \{\uparrow, \downarrow\}$). The left reservoir and its coupling to the system are described in an analogous manner. We first consider the left and right reservoirs to have a common chemical potential, $\mu_{\rm res}$.

In general, the values of the couplings J_{lp} depend on the precise forms of the reservoir states $|l\rangle$, and the details of the lead-system coupling. We take the couplings to be uniform in the $\hat{\boldsymbol{x}}$ direction; for the right lead, we specify $J_{lp} = J\delta_{yL_y}\delta_{\nu(p)\nu(l)}\delta_{k_x(p)k_x(l)}$. For the left lead, we replace δ_{yL_y} with δ_{y0}. (We do not expect our results to change qualitatively for other generic forms of the reservoirs and the couplings.)

In the following we will consider the effect of the leads when $\mu_{\rm res}$ is placed within the Floquet gap. Note that a Floquet state of the system with quasienergy ε is coupled to reservoir states in a wide range of energies $\mathcal{E}_l = \varepsilon + n\hbar\Omega$ via the harmonics $|\chi^n_{k_x\beta}\rangle$ (or $|\phi^n_{\boldsymbol{k}\alpha}\rangle$). As a result, if the reservoir's density of states has a wide bandwidth, electrons occupying lead states below the Fermi level can tunnel into the upper Floquet band of the system. These processes (and similar processes for holes) increase the number of excited particles (holes) in the upper (lower) Floquet band, leading to deviations from the ideal Floquet insulator state. To avoid this deleterious effect, we couple the Fermi reservoir through a narrow band of "filter" states [43,58–60], which effectively limits the density of states of the Fermi reservoir. In our simulation, we take the reservoirs to have a box-shaped DOS of width w, aligned symmetrically around the center of a single Floquet zone, see Fig. 1.

The introduction of the system-lead coupling, $\hat{\mathcal{H}}^{R(L)}_{\rm res}$, adds additional collision integrals to the Boltzmann equations for the bulk and edge distributions. The collision integral describing scattering between the right reservoir and the right edge state is given by

$$\mathcal{I}^{\rm e,res}_{k_x{\rm R}} = \sum_n \mathcal{J}^n_{k_x{\rm R}}\big[f_{\rm FD}\big(\varepsilon^n_{\rm R}(k_x) - \mu_{\rm res}\big) - f^{\rm e}_{k_x{\rm R}}\big]. \quad (13)$$

Here, $\mathcal{J}^n_{k_x{\rm R}} = \frac{2\pi}{\hbar}|J|^2\sum_{l,\nu}|\langle k_x, L_y, \nu|\chi^n_{k_x;{\rm R}}\rangle|^2\delta(\varepsilon^n_{\rm R}(k_x) - \mathcal{E}_l)$, where $|k_x, L_y, \nu\rangle$ is the state created by $c^\dagger_{k_x, y=L_y, \nu}$ and $\varepsilon^n_{\rm R}(k_x) = \varepsilon_{\rm R}(k_x) + n\hbar\Omega$; $\varepsilon_{\rm R}(k_x)$ is the quasienergy of the right edge state, with quasimomentum k_x. The values of $\mathcal{E}_l$ are limited to the range within the filter window. An identical expression holds for the left edge state, with ${\rm R} \to {\rm L}$. In addition, Eq. (9) contains a collision integral $\mathcal{I}^{\rm b,res}_{\boldsymbol{k}\alpha}$ describing scattering directly between the leads and the bulk states. The rates appearing in this collision integral are significant only for y values sufficiently close to the leads (see Appendix A).

The coupling strength between the reservoir and the edge states is characterized by $\overline{\mathcal{J}}_\beta = \frac{1}{2k_R}\int_{-k_R}^{k_R} dk_x \mathcal{J}^0_{k_x;\beta}$. When $\overline{\mathcal{J}}_\beta \gg \Lambda^{{\rm e}\to{\rm b}} n_{\rm b}$ (such that tunneling between the reservoir and the edge states dominates over scattering from the edge states to the bulk), we expect the distribution of the edge states to be described by the quasi Fermi-Dirac distribution $f_{\rm QFD}$, with an effective chemical potential $\mu_{\rm e}$, which is pinned to $\mu_{\rm res}$.[6] In contrast, we expect the total density of bulk excitations $\bar{n}_{\rm b} = n_+ + n_-$ to remain constant when $\mu_{\rm res}$ is changed, as long as $\mu_{\rm res}$ remains within the Floquet gap. (The densities n_+ and n_- correspond to the densities of electrons and holes in the upper and lower Floquet bands, respectively.) In Fig. 4(a), we plot $\mu_{\rm e}$, as well as $\bar{n}_{\rm b}(\mu_{\rm res})/\bar{n}_{\rm b}(\mu_{\rm res} = 0)$, as a function of $\mu_{\rm res}$. The numerical results plotted in Fig. 4(a) indeed show the "incompressible" behavior of the bulk excitation density, and the pinning of $\mu_{\rm e}$ on the edge to the chemical potential of the reservoir.

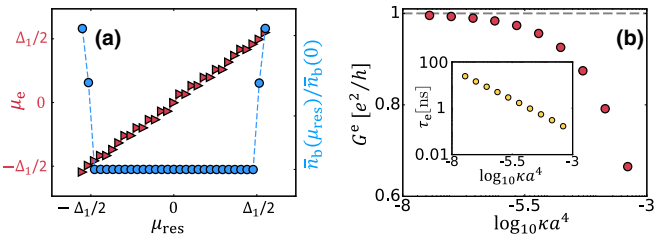

FIG. 4. (a) The effective chemical potential of the right edge, $\mu_{\rm e}$ (triangles), and the total normalized excitation density in the bulk, $\bar{n}_{\rm b}(\mu_{\rm res})/\bar{n}_{\rm b}(\mu_{\rm res} = 0)$ (circles), for a system coupled to filtered Fermi reservoirs near the left and the right edges as a function of the common chemical potential of the two leads, $\mu_{\rm res}$. The system-lead couplings are taken to be $\overline{\mathcal{J}}_{\rm R}, \overline{\mathcal{J}}_{\rm L} \approx 2.4\Lambda^{{\rm e}\to{\rm b}} n_{\rm b}$, and for their filter bandwidths we take $w = \hbar\Omega$. The chemical potential $\mu_{\rm e}$ is computed by fitting the edge distribution to a quasi Fermi-Dirac distribution $f_{\rm QFD}$. (b) The edge contribution to two-terminal conductance as a function of κa^4, for sample size $L_y = 5$ μm, and Fermi velocity, $v_{\rm e} \approx 10^5$ m/sec. The conductance approaches the quantum limit, e^2/h, as $\kappa a^4 \to 0$. (Inset) The lifetime of the edge states due to edge-to-bulk scattering processes ($\tau_{\rm e}$). The lifetime scales with κ as $\tau_{\rm e} \sim (\kappa a^4)^{-0.51}$.

[6] The coupling to an energy filtered Fermi reservoir also affects the effective temperature and the δ-parameter of the steady state.

VIII. EDGE STATE TRANSPORT

We consider a two-terminal transport measurement using a bar geometry, when a voltage bias $\Delta\mu = \mu^{\rm R}_{\rm res} - \mu^{\rm L}_{\rm res}$ is applied between the leads [see Fig. 2(b)]. The current through an FTI should in general have both bulk and edge contributions, characterized by a total conductance of the form $G = G^{\rm e} + (L_x/L_y)\sigma^{\rm b}_{yy}$.[7] To estimate $G^{\rm e}$, we consider an excess charge density on the right-moving edge due to occupation of edge modes with $\varepsilon > 0$. We denote this quantity by $\Delta n_{\rm e}$. The continuity equation for $\Delta n_{\rm e}$ is given by $\partial_t \Delta n_{\rm e} = -v_{\rm e}\partial_y \Delta n_{\rm e} - (\Delta n_{\rm e} - n_{\rm e})/\tau_{\rm e}$, where $v_{\rm e}$ is the edge velocity, $\tau_{\rm e}$ is lifetime of the edge excitations, and $n_{\rm e}$ is the density of excitations on the right-moving edge, far away from the leads, see Eq. (7). We define $\Delta n_{\rm e}$ for the left movers accordingly. The lifetime $\tau_{\rm e}$ is determined predominantly by edge-to-bulk scattering processes, such that $\tau_{\rm e} \approx (\Lambda^{{\rm e}\to{\rm b}} n_{\rm b})^{-1} \sim \kappa^{-\frac{1}{2}}$. Assuming that the leads set the boundary conditions for $\Delta n_{\rm e}$ at $y = 0$ and $y = L_y$, for the right and left movers, correspondingly, we estimate the edge contribution to the two-terminal conductance: $G^{\rm e} = (e^2/h)(1-\delta)e^{-L_y/\tau_{\rm e} v_{\rm e}}$ (see Appendix E). Figure 4(b) displays the numerically obtained values of $\tau_{\rm e}$, and the corresponding estimate for $G^{\rm e}$ as a function of κ. As $\kappa \to 0$, $\tau_{\rm e}$ increases and δ decreases; thus the conductance $G^{\rm e}$ approaches the quantum limit e^2/h.

IX. DISCUSSION

To estimate physically accessible values of κ, we associate the phonon and photon mediated transitions with the typically observed hot electron lifetime, $\tau_{\rm he} \sim 0.1$ ps [61], and the radiative recombination lifetime, $\tau_{\rm rr} \sim 0.1$ ns, respectively. For $A_{\mathcal{R}} a^2 \sim 10^{-2}$, we then estimate $\kappa_* a^4 \approx \frac{A_{\mathcal{R}} a^2}{(2\pi)^2}\frac{\tau_{\rm he}}{\tau_{\rm rr}} \sim 10^{-6}$. As seen in Fig. 4(b), for this value of κ and a sample of the size $L_y = 1\,\mu$m, $G^{\rm e}$ is within a few percent of the quantized value.

The bulk contribution to the conductivity $\sigma^{\rm b}_{yy}$ will naturally depend on the material used to implement the FTI. Prominent candidates are CdTe/HgTe and InAs/GaSb heterostructures [7], and honeycomb lattice materials such as transition-metal dichalcogenides [62], and graphene [32]. The low-temperature mobilities of these materials vary over a range of a few orders of magnitude [63]. Lower mobility samples, in which the bulk conductance is suppressed, may be advantageous for measurements of $G^{\rm e}$. We evaluate the bulk conductivity as $\sigma^{\rm b}_{yy} \approx 2e\mu n_{\rm b} \approx (e^2/h)(\mu/\mu_*)(\kappa/\kappa_*)^{\frac{1}{2}}$, where μ is the mobility and $\mu_* = \frac{e}{2h\kappa_*^{1/2}} \sim 400$ cm^2/(V sec).[8] The bulk may also exhibit an anomalous Hall effect due to the nonzero Berry curvature of the Floquet bands. The Hall conductivity for low κ is of the order of e^2/h and may be further renormalized by disorder [64].

Our results demonstrate that the topological properties of the band structures of FTIs, and in particular the existence of edge states, can be manifested in an experimentally accessible transport measurement. To fully explore the possibilities offered by FTIs, other methods for detecting the edge states need to be developed. These may include position dependent spectroscopic and magnetic probes [65–68], as well as interference measurements between edge modes [69]. Investigating the role of interparticle collisions in the driven system [45,70–72] is also an important direction for future study.

[7] This formula applies also when $\sigma^{\rm b}_{xy} \neq 0$ [76].

[8] The mobility includes both phonon and impurity scattering, see Appendix E.

ACKNOWLEDGMENTS

We thank Vladimir Kalnizky, Barak Katzir, Gali Matsman, and Ari Turner for illuminating discussions, and David Cohen for technical support. N.L. acknowledges support from the European Research Council (ERC) under the European Union Horizon 2020 Research and Innovation Programme (Grant Agreement No. 639172), from the People Programme (Marie Curie Actions) of the European Union's Seventh Framework Programme (FP7/2007–2013), under REA Grant Agreement No. 631696, and from the Israeli Center of Research Excellence (I-CORE) "Circle of Light" funded by the Israel Science Foundation (Grant No. 1802/12). M.R. gratefully acknowledges the support of the European Research Council (ERC) under the European Union Horizon 2020 Research and Innovation Programme (Grant Agreement No. 678862), and the Villum Foundation. G.R. acknowledges support from the U. S. Army Research Office under Grant No. W911NF-16-1-0361, and from the IQIM, an NSF frontier center funded in part by the Betty and Gordon Moore Foundation. We also thank the Aspen Center for Physics, which is supported by National Science Foundation grant PHY-1607611 where part of the work was done.

APPENDIX A: DERIVATION OF THE BOLTZMANN KINETIC EQUATION

In this section, we derive the Boltzmann equation for the system described in Eqs. (1)–(4). We define the phase space distribution in the bulk, $f^{\rm b}_{\boldsymbol{k}\alpha}(\boldsymbol{r};t)$ [see Eq. (8)] through the Keldysh component of the Green function, $\mathcal{G}^K_\alpha = (1 - 2f^{\rm b}_\alpha)(\mathcal{G}^R_\alpha - \mathcal{G}^A_\alpha)$. As in the main text, $\alpha = +,-$ denotes the upper and lower Floquet bands, respectively. The Green's function $\mathcal{G}_\alpha$ satisfies the Dyson equation [73,74],

$$\left(G^{-1}_\alpha - \Sigma_\alpha\right) \circ \mathcal{G}_\alpha = \mathbb{1}. \tag{A1}$$

We write Eq. (A1) for Wigner-transformed functions, $\mathcal{G}_\alpha(\boldsymbol{k},\boldsymbol{r};\omega,t)$, $G_\alpha(\boldsymbol{k},\boldsymbol{r};\omega,t)$, and $\Sigma_\alpha(\boldsymbol{k},\boldsymbol{r};\omega,t)$. In this representation, $\circ \equiv \exp\{\frac{i}{2}(\overleftarrow{\partial}_{\boldsymbol{r}}\overrightarrow{\partial}_{\boldsymbol{k}} - \overleftarrow{\partial}_{\boldsymbol{k}}\overrightarrow{\partial}_{\boldsymbol{r}}) - \frac{i}{2}(\overleftarrow{\partial}_t\overrightarrow{\partial}_\omega - \overleftarrow{\partial}_\omega\overrightarrow{\partial}_t)\}$ denotes the Moyal operator (the arrows denote whether the derivative acts to the left or the right). The two-point functions over the Keldysh time contour, $\mathcal{G}_\alpha$, G_α, and Σ_α are arranged in a matrix form, for instance, $\mathcal{G}_\alpha = \begin{pmatrix} \mathcal{G}^R_\alpha & \mathcal{G}^K_\alpha \\ 0 & \mathcal{G}^A_\alpha \end{pmatrix}$ [75], and similarly for G_α and Σ_α. Here, G_α is the free propagator whose inverse is given by $[G^{-1}_\alpha]^{R/A} = \omega - \varepsilon_\alpha(\boldsymbol{k})/\hbar \pm i0^+$, $[G^{-1}_\alpha]^K \approx 0$ (note that G_α is independent of $\boldsymbol{r}$ and t). The full form of the self-energy Σ_α appearing in Eq. (A1) will be given below.

The distribution of electrons in the edge states, $f^{\rm e}_{k_x\beta}(t)$ [see below Eq. (8)], is defined through the Keldysh component of the edge Green function $\tilde{\mathcal{G}}^K_\beta = (1 - 2f^{\rm e}_\beta)(\tilde{\mathcal{G}}^R_\beta - \tilde{\mathcal{G}}^A_\beta)$. As in the main text, $\beta = {\rm R}, {\rm L}$ denotes the right and left edge states. The

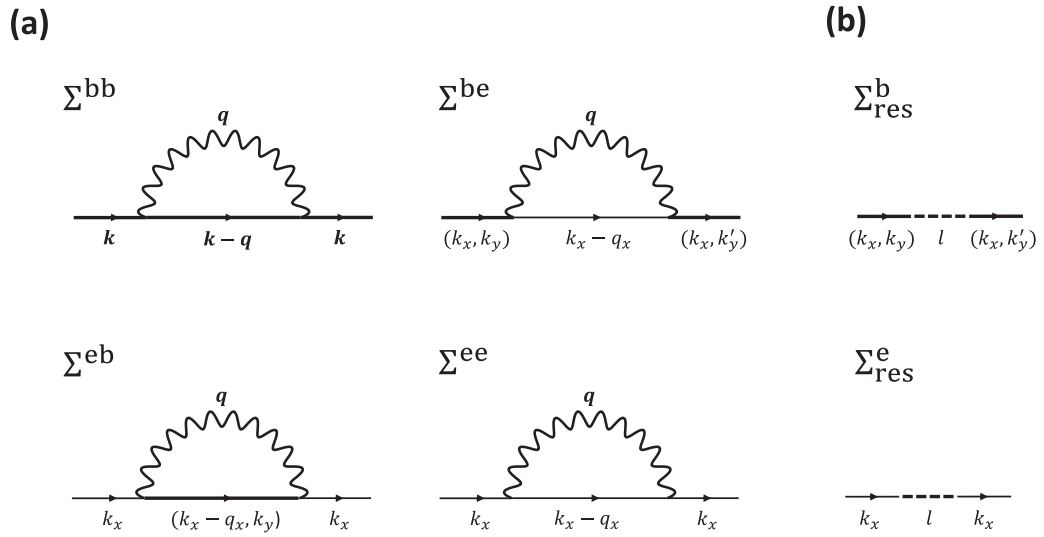

FIG. 5. Diagrams that lead to the self-energy, (a) due to electron-boson collision processes; (b) due to system-lead tunneling. Bold and thin full lines correspond to bulk and edge propagators, respectively; wiggly and dashed lines denote the propagators of bosons and particles in the lead.

edge Green's function $\tilde{\mathcal{G}}_\beta$ satisfies the Dyson equation [73,74],

$$\left(\tilde{G}_\beta^{-1} - \tilde{\Sigma}_\beta\right) \diamond \tilde{\mathcal{G}}_\beta = \mathbb{1}, \tag{A2}$$

where due to translation invariance in the x direction, $\diamond \equiv \exp[-\frac{i}{2}(\overleftarrow{\partial}_t \overrightarrow{\partial}_\omega - \overleftarrow{\partial}_\omega \overrightarrow{\partial}_t)]$. The functions $\tilde{\mathcal{G}}_\beta(k_x;\omega,t)$, $\tilde{G}_\beta(k_x;\omega,t)$, and $\tilde{\Sigma}_\beta(k_x;\omega,t)$ are arranged in a matrix form in a similar manner to the bulk Green's functions. The free propagator for the edge states is given by $[\tilde{G}_\beta^{-1}]^{R/A} = \omega - \varepsilon_\beta(k_x)/\hbar \pm i0^+$ and $[\tilde{G}_\beta^{-1}]^K \approx 0$.

The bulk self-energy Σ_α in Eq. (A1) has contributions from both bulk-bulk and bulk-edge scattering, $\Sigma_\alpha = \Sigma_\alpha^{bb} + \Sigma_\alpha^{be}$. We expand the self-energy to the second order in the electron-boson coupling. At this order, the diagrams that lead to the self-energy appear in Fig. 5(a). In the following derivation, we will use the notation $|\phi^n_{k\alpha}\rangle$ and $|\chi^n_{k_x\beta}(y)\rangle$ for the bulk and edge states appearing in the Fourier decomposition of Floquet states, see the discussion below Eq. (2). Notice that $|\phi^n_{k\alpha}\rangle$ and $|\chi^n_{k_x\beta}(y)\rangle$ are spinors in the pseudospin basis. For bulk-bulk scattering, the Wigner transform of the self-energy Σ_α^{bb} is given by

$$\Sigma^{bb}_{\alpha,\lambda}(\boldsymbol{k},y;\omega,t) = \frac{2\pi i}{\hbar} a^3 \int \frac{d\omega' d^3\boldsymbol{q}}{(2\pi)^4} \frac{1}{L_x L_y} \sum_{n,\alpha'\boldsymbol{k}'} \left| \sum_m \langle \phi^m_{\boldsymbol{k}\alpha} | \eta_\lambda | \phi^{m-n}_{\boldsymbol{k}'\alpha'} \rangle \right|^2 (2\pi)^2 \delta^{(2)}(\boldsymbol{k} - \boldsymbol{k}' - \boldsymbol{q})$$
$$\times \sum_{v,v'\in\{q,cl\}} \gamma^v \mathcal{G}_{\alpha'}(\boldsymbol{k}',y;\omega-\omega'-n\Omega,t)\gamma^{v'}[D_{vv'}(\boldsymbol{q},\omega') + D^*_{v'v}(-\boldsymbol{q},-\omega')]. \tag{A3}$$

Here, $\eta_s = g_s\mathbb{1}$, $\eta_\ell = g_\ell\sigma^+$ [see Eq. (4)], $\gamma^q = \frac{1}{2}\mathbb{1}$, $\gamma^{cl} = \frac{1}{2}\sigma^x$ are the vertex fermionic matrices [74]; the functions $D_{vv'}$ are given by $D_{cl,q} = \frac{1}{\omega - v_\lambda|\boldsymbol{q}| \pm i0^+}$, $D_{q,cl} = D^*_{cl,q}$, and $D_{cl,cl} = \coth(\frac{\hbar\omega}{2k_BT})(D_{cl,q} - D_{q,cl})$, is the free bosonic propagator; $\delta^{(2)}(\boldsymbol{k} - \boldsymbol{k}' - \boldsymbol{q})$ enforces momentum conservation in the two-dimensional plane of the system. Expanding the self-energy to leading order, we approximate on the right-hand side of Eq. (A3) $\mathcal{G}^{R/A}_\alpha \approx G^{R/A}_\alpha$.

For bulk-edge scattering, the Wigner transform of the self-energy Σ_α^{be} is given by

$$\Sigma^{be}_{\alpha,\lambda}(\boldsymbol{k},y;\omega,t) = \frac{2\pi i}{\hbar} a^3 \int \frac{d\omega' d^3\boldsymbol{q}}{(2\pi)^4} \frac{1}{L_x} \sum_{n,\beta' k'_x} \zeta^{k'_x\beta'}_{n,\boldsymbol{k}\alpha}(q_y,y)(2\pi)\delta^{(1)}(k_x - k'_x - q_x) \sum_{v,v'\in\{q,cl\}} \gamma^v \tilde{\mathcal{G}}_{\beta'}(k'_x;\omega-\omega'-n\Omega,t)\gamma^{v'}$$
$$\times [D_{vv'}(\boldsymbol{q},\omega') + D^*_{v'v}(-\boldsymbol{q},-\omega')]. \tag{A4}$$

where we have defined

$$\zeta^{k'_x\beta'}_{n,\boldsymbol{k}\alpha}(q_y,y) = \int \frac{d\bar{k}_y}{a\pi} e^{2i\bar{k}_y y} \int d\bar{y} e^{-i(k_y+\bar{k}_y-q_y)\bar{y}} \sum_m \langle \phi^m_{\boldsymbol{k}+\bar{k}_y\hat{\boldsymbol{y}}\alpha} | \eta_\lambda | \chi^{m-n}_{k'_x\beta'}(\bar{y}) \rangle \int d\bar{y}' e^{i(k_y-\bar{k}_y-q_y)\bar{y}'} \sum_m \langle \chi^{m-n}_{k'_x\beta'}(\bar{y}') | \eta^\dagger_\lambda | \phi^m_{\boldsymbol{k}-\bar{k}_y\hat{\boldsymbol{y}}\alpha} \rangle. \tag{A5}$$

Since the edge states are localized in y, $\zeta^{k'_x\beta'}_{n,\boldsymbol{k}\alpha}(y)$ has a compact support near the position of the edges.

The edge self-energy $\tilde{\Sigma}_\beta$ in Eq. (A2) has contributions from both edge-bulk and edge-edge scattering, $\tilde{\Sigma}_\beta = \Sigma^{\rm eb}_\beta + \Sigma^{\rm ee}_\beta$. The Wigner transforms of these self-energies read

$$\Sigma^{\rm eb}_{\beta,\lambda}(k_x;\omega,t) = \frac{2\pi i}{\hbar}a^3\int\frac{d\omega' d^3\boldsymbol{q}}{(2\pi)^4}\frac{a}{L_y}\sum_{n,\alpha'\boldsymbol{k}'y}\tilde{\xi}^{\boldsymbol{k}'\alpha'}_{n,k_x\beta}(q_y,y)(2\pi)\delta^{(1)}(k_x-k'_x-q_x)\sum_{v,v'\in\{\rm q,cl\}}\gamma^v\mathcal{G}_{\alpha'}(\boldsymbol{k}',y;\omega-\omega'-n\Omega,t)\gamma^{v'}$$
$$\times[D_{vv'}(\boldsymbol{q},\omega')+D^*_{v'v}(-\boldsymbol{q},-\omega')], \tag{A6}$$

$$\Sigma^{\rm ee}_{\beta,\lambda}(k_x;\omega,t) = \frac{2\pi i}{\hbar}a^3\int\frac{d\omega' d^3\boldsymbol{q}}{(2\pi)^4}\frac{1}{L_x}\sum_{n,\beta'k'_x}\left|\sum_m\langle\chi^m_{k_x\beta}|\eta_\lambda|\chi^{m-n}_{k'_x\beta'}\rangle\right|^2(2\pi)\delta^{(1)}(k_x-k'_x-q_x)\sum_{v,v'\in\{\rm q,cl\}}\gamma^v\tilde{\mathcal{G}}_{\beta'}(k'_x;\omega-\omega'-n\Omega,t)\gamma^{v'}$$
$$\times[D_{vv'}(\boldsymbol{q},\omega')+D^*_{v'v}(-\boldsymbol{q},-\omega')], \tag{A7}$$

where

$$\tilde{\xi}^{\boldsymbol{k}'\alpha'}_{n,k_x\beta}(q_y,y) = \int\frac{d\bar{k}_y}{a\pi}e^{2i\bar{k}_y y}\int d\bar{y}e^{i(k_y+\bar{k}_y+q_y)\bar{y}}\sum_m\langle\chi^m_{k'_x\beta'}(\bar{y})|\eta_\lambda|\phi^{m-n}_{\boldsymbol{k}+\bar{k}_y\hat{\boldsymbol{y}}\alpha}\rangle\int d\bar{y}'e^{-i(k_y-\bar{k}_y+q_y)\bar{y}'}\sum_m\langle\phi^{m-n}_{\boldsymbol{k}-\bar{k}_y\hat{\boldsymbol{y}}\alpha}|\eta^\dagger_\lambda|\chi^m_{k'_x\beta'}(\bar{y}')\rangle. \tag{A8}$$

Equations (A1) and (A2) are the kinetic equations for the Floquet bulk and edge states, written in the matrix form. Writing the explicit expressions for the Keldysh matrices $G_\alpha, \mathcal{G}_\alpha$, and Σ_α in terms of their components, we arrive at three independent equations, that for the bulk Green's functions read

$$\left([G^{-1}_\alpha]^R-\Sigma^R_\alpha\right)\circ\mathcal{G}^R_\alpha = \mathbb{1}, \tag{A9a}$$
$$\left([G^{-1}_\alpha]^A-\Sigma^A_\alpha\right)\circ\mathcal{G}^A_\alpha = \mathbb{1}, \tag{A9b}$$
$$\left([G^{-1}_\alpha]^R-\Sigma^R_\alpha\right)\circ\mathcal{G}^K_\alpha+\left([G^{-1}_\alpha]^K-\Sigma^K_\alpha\right)\circ\mathcal{G}^A_\alpha = 0. \tag{A9c}$$

Using Eqs. (A9a)–(A9c) and neglecting derivatives of Σ, assuming no spatial variations on the lattice lengthscale, we arrive at

$$[G^{-1}_\alpha]^R\circ f^{\rm b}_\alpha - f^{\rm b}_\alpha\circ[G^{-1}_\alpha]^A \approx \frac{1}{2}\left[\Sigma^K_\alpha-\left(\Sigma^R_\alpha-\Sigma^A_\alpha\right)\left(1-2f^{\rm b}_\alpha\right)\right]. \tag{A10}$$

This equation can be further simplified to the form of the Boltzmann equation (Eq. (9)) by evaluating the left-hand side of Eq. (A10), which gives $[G^{-1}_\alpha]^R\circ f^{\rm b}_\alpha - f^{\rm b}_\alpha\circ[G^{-1}_\alpha]^A \approx i\partial_t f^{\rm b}_\alpha + (i/\hbar)\partial_{\boldsymbol{k}}\varepsilon_\alpha(\boldsymbol{k})\partial_{\boldsymbol{r}} f^{\rm b}_\alpha$, where we neglected higher order derivatives of f. The equation for the edge has a similar form, $[\tilde{G}^{-1}_\beta]^R\diamond f^{\rm e}_\beta - f^{\rm e}_\beta\diamond[\tilde{G}^{-1}_\beta]^A \approx i\partial_t f^{\rm e}_\beta$. The right-hand side of Eq. (A10) gives the collision integral appearing in the Boltzman equation, Eq. (A10),

$$\mathcal{I} = -\frac{i}{2}[\Sigma^K-(\Sigma^R-\Sigma^A)(1-2f)]\Big|_{\hbar\omega=\varepsilon_\alpha(\boldsymbol{k})}. \tag{A11}$$

1. Explicit expressions for the edge and the bulk collision integrals

We now present explicit expressions for the Boltzmann equation for the bulk and the edge states, for zero dc electric field,

$$\partial_t f^{\rm b}_{\boldsymbol{k}\alpha}+v_{y,\alpha}(\boldsymbol{k})\partial_y f^{\rm b}_{\boldsymbol{k}\alpha} = \mathcal{I}^{\rm bb}_{\boldsymbol{k}\alpha}(y)+\mathcal{I}^{\rm bR}_{\boldsymbol{k}\alpha}(y)+\mathcal{I}^{\rm bL}_{\boldsymbol{k}\alpha}(y), \tag{A12a}$$
$$\partial_t f^{\rm e}_{k_x\beta} = \mathcal{I}^{\rm ee}_{k_x\beta}+\mathcal{I}^{\rm eb}_{k_x\beta}, \tag{A12b}$$

where $v_{y,\alpha}(\boldsymbol{k}) = \hbar^{-1}\partial_{k_y}\varepsilon_\alpha(\boldsymbol{k})$, and the collision integrals are

$$\mathcal{I}^{\rm bb}_{\boldsymbol{k}\alpha}(y) = \sum_{n,\boldsymbol{k}'\alpha'}\left[W^{{\rm bb},\boldsymbol{k}'\alpha'}_{n,\boldsymbol{k}\alpha}\mathscr{F}^{{\rm bb},\boldsymbol{k}'\alpha'}_{n,\boldsymbol{k}\alpha}(y)-W^{{\rm bb},\boldsymbol{k}\alpha}_{n,\boldsymbol{k}'\alpha'}\mathscr{F}^{{\rm bb},\boldsymbol{k}\alpha}_{n,\boldsymbol{k}'\alpha'}(y)\right], \tag{A13a}$$

$$\mathcal{I}^{{\rm b}\beta}_{\boldsymbol{k}\alpha}(y) = \sum_{n,k'_x}\left[W^{{\rm be},k'_x\beta}_{n,\boldsymbol{k}\alpha}(y)\mathscr{F}^{{\rm be},k'_x\beta}_{n,\boldsymbol{k}\alpha}(y)-W^{{\rm eb},\boldsymbol{k}\alpha}_{n,k'_x\beta}(y)\mathscr{F}^{{\rm eb},\boldsymbol{k}\alpha}_{n,k'_x\beta}(y)\right], \tag{A13b}$$

$$\mathcal{I}^{\rm ee}_{k_x\beta} = \sum_{n,k'_x\beta'}\left[W^{{\rm ee},k'_x\beta'}_{n,k_x\beta}\mathscr{F}^{{\rm ee},k'_x\beta'}_{n,k_x\beta}-W^{{\rm ee},k_x\beta}_{n,k'_x\beta'}\mathscr{F}^{{\rm ee},k_x\beta}_{n,k'_x\beta'}\right], \tag{A13c}$$

$$\mathcal{I}^{\rm eb}_{k_x\beta} = \frac{a}{L_y}\sum_{n,\boldsymbol{k}'\alpha',y}\left[W^{{\rm eb},\boldsymbol{k}'\alpha'}_{n,k_x\beta}(y)\mathscr{F}^{{\rm eb},\boldsymbol{k}'\alpha'}_{n,k_x\beta}(y)-W^{{\rm be},k_x\beta}_{n,\boldsymbol{k}'\alpha'}(y)\mathscr{F}^{{\rm be},k_x\beta}_{n,\boldsymbol{k}'\alpha'}(y)\right]. \tag{A13d}$$

Where we defined, for brevity,

$$\mathscr{F}^{\varrho\varrho',\boldsymbol{k}'\alpha'}_{n,\boldsymbol{k}\alpha} = \left[1-f^{\varrho}_{\boldsymbol{k}\alpha}\right]f^{\varrho'}_{\boldsymbol{k}'\alpha'}N^{\boldsymbol{k}'\alpha'}_{n,\boldsymbol{k}\alpha}-f^{\varrho}_{\boldsymbol{k}\alpha}\left[1-f^{\varrho'}_{\boldsymbol{k}'\alpha'}\right]\left(1+N^{\boldsymbol{k}'\alpha'}_{n,\boldsymbol{k}\alpha}\right), \tag{A14}$$

$N^{\boldsymbol{k}'\alpha'}_{n,\boldsymbol{k}\alpha} = [\exp(\frac{\varepsilon_\alpha(\boldsymbol{k})-\varepsilon_{\alpha'}(\boldsymbol{k}')+n\hbar\Omega}{k_{\rm B}T})-1]^{-1}$, and each rate, $W^{\varrho\varrho',\boldsymbol{k}'\alpha'}_{n,\boldsymbol{k}\alpha}$, is a sum of phonons and photons, $W^{\varrho\varrho',\boldsymbol{k}'\alpha'}_{n,\boldsymbol{k}\alpha} = W^{\varrho\varrho',\boldsymbol{k}'\alpha'}_{\ell,n,\boldsymbol{k}\alpha}+W^{\varrho\varrho',\boldsymbol{k}'\alpha'}_{s,n,\boldsymbol{k}\alpha}$ for ϱ and $\varrho' = \{\rm b,e\}$ denoting the bulk and edge, respectively. Notice that we have introduced additional indices for W relative

to the definition in the main text, where we showed the expression for bulk-to-bulk collisions only (i.e., $\varrho = \varrho' = \mathrm{b}$). Explicit expressions for these rates can be derived from Eqs. (A3), (A4), (A6), and (A7), yielding

$$W^{\mathrm{bb},\boldsymbol{k}'\alpha'}_{\lambda,n,\boldsymbol{k}\alpha} = \frac{2\pi}{\hbar}\frac{1}{L_x L_y}\int a^3 d^3\boldsymbol{q}\left|\sum_m \langle\phi^m_{\boldsymbol{k}\alpha}|\eta_\lambda|\phi^{m-n}_{\boldsymbol{k}'\alpha'}\rangle\right|^2 \delta(\varepsilon_\alpha(\boldsymbol{k}) - \varepsilon_{\alpha'}(\boldsymbol{k}') - \hbar v_\lambda|\boldsymbol{q}| + n\hbar\Omega)\delta^{(2)}(\boldsymbol{k} - \boldsymbol{k}' + \boldsymbol{q}), \tag{A15a}$$

$$W^{\mathrm{be},k'_x\beta'}_{\lambda,n,\boldsymbol{k}\alpha}(y) = \frac{2\pi}{\hbar}\frac{1}{L_x}\int \frac{a^3 d^3\boldsymbol{q}}{2\pi}\zeta^{k'_x\beta'}_{n,\boldsymbol{k}\alpha}(q_y,y)\delta(\varepsilon_\alpha(\boldsymbol{k}) - \varepsilon_{\beta'}(k'_x) - \hbar v_\lambda|\boldsymbol{q}| + n\hbar\Omega)\delta^{(1)}(k_x - k'_x + \boldsymbol{q}), \tag{A15b}$$

$$W^{\mathrm{ee},k'_x\beta'}_{\lambda,n,k_x\beta} = \frac{2\pi}{\hbar}\frac{1}{L_x}\int \frac{a^3 d^3\boldsymbol{q}}{2\pi}\left|\sum_m \langle\chi^m_{k_x\beta}|\eta_\lambda|\chi^{m-n}_{k'_x\beta'}\rangle\right|^2 \delta(\varepsilon_\beta(k_x) - \varepsilon_{\beta'}(k'_x) - \hbar v_\lambda|\boldsymbol{q}| + n\hbar\Omega)\delta^{(1)}(k_x - k'_x + \boldsymbol{q}), \tag{A15c}$$

$$W^{\mathrm{eb},\boldsymbol{k}'\alpha'}_{\lambda,n,k_x\beta}(y) = \frac{2\pi}{\hbar}\frac{1}{L_x}\int \frac{a^3 d^3\boldsymbol{q}}{2\pi}\tilde{\zeta}^{\boldsymbol{k}'\alpha'}_{n,k_x\beta}(q_y,y)\delta(\varepsilon_\beta(k_x) - \varepsilon_{\alpha'}(\boldsymbol{k}') - \hbar v_\lambda|\boldsymbol{q}| + n\hbar\Omega)\delta^{(1)}(k_x - k'_x + \boldsymbol{q}). \tag{A15d}$$

To obtain useful expressions for the simulation, we need to make assumptions on the profile of the edge wave functions, $|\chi^n_{k_x,\beta}\rangle$ as function of y. This will set closed expressions for ζ functions. Since our discretization of the real space is larger then the localization length of the edge, we can simplify Eqs. (A15b) and (A15d) by assuming edge states exponentially localized on the length of the order of the lattice spacing. For simplicity, we take, $|\chi^n_{k_x,\beta}(y)\rangle = \delta_{y,0}|\bar{\chi}^n_{k_x,\beta}\rangle$. This approximation does not effect our numerical results, since in our simulation we discretize the y direction on a length scale of the healing length, which is much larger then the lattice scale (see Section C). In this limit, we obtain

$$\zeta^{k'_x\beta'}_{n,\boldsymbol{k}\alpha}(q_y,y) = \delta_{y,0}\left|\sum_m \langle\phi^m_{\boldsymbol{k}\alpha}|\eta_\lambda|\bar{\chi}^{m-n}_{k'_x\beta'}\rangle\right|^2 \tag{A16}$$

independent of q_y. Then the expressions for the rates can be written in the form

$$W^{\mathrm{bb},\boldsymbol{k}'\alpha'}_{\lambda,n,\boldsymbol{k}\alpha} = \frac{2\pi}{\hbar}\left|\sum_m \langle\phi^m_{\boldsymbol{k}\alpha}|\eta_\lambda|\phi^{m-n}_{\boldsymbol{k}'\alpha'}\rangle\right|^2 \times \rho^{\mathrm{b}}_\lambda(\varepsilon_\alpha(\boldsymbol{k}) - \varepsilon_{\alpha'}(\boldsymbol{k}') + n\hbar\Omega, \boldsymbol{k} - \boldsymbol{k}'), \tag{A17a}$$

$$W^{\mathrm{be},k'_x\beta'}_{\lambda,n,\boldsymbol{k}\alpha} = \frac{2\pi}{\hbar}\delta_{y,0}\left|\sum_m \langle\phi^m_{\boldsymbol{k}\alpha}|\eta_\lambda|\bar{\chi}^{m-n}_{k'_x\beta'}\rangle\right|^2 \times \rho^{\mathrm{e}}_\lambda(\varepsilon_\alpha(\boldsymbol{k}) - \varepsilon_{\beta'}(k'_x) + n\hbar\Omega, k_x - k'_x), \tag{A17b}$$

$$W^{\mathrm{ee},k'_x\beta'}_{\lambda,n,k_x\beta} = \frac{2\pi}{\hbar}\left|\sum_m \langle\chi^m_{k_x\beta}|\eta_\lambda|\chi^{m-n}_{k'_x\beta'}\rangle\right|^2 \times \rho^{\mathrm{e}}_\lambda(\varepsilon_\beta(k_x) - \varepsilon_{\beta'}(k'_x) + n\hbar\Omega, k_x - k'_x), \tag{A17c}$$

$$W^{\mathrm{eb},\boldsymbol{k}'\alpha'}_{\lambda,n,k_x\beta} = \frac{2\pi}{\hbar}\delta_{y,0}\left|\sum_m \langle\bar{\chi}^m_{k_x\beta}|\eta_\lambda|\phi^{m-n}_{\boldsymbol{k}'\alpha'}\rangle\right|^2 \times \rho^{\mathrm{e}}_\lambda(\varepsilon_\alpha(\boldsymbol{k}) - \varepsilon_{\beta'}(k'_x) + n\hbar\Omega, k_x - k'_x), \tag{A17d}$$

where

$$\rho^{\mathrm{b}}_\lambda(\varepsilon,\boldsymbol{q}) = \frac{a^2}{L_x L_y}\frac{a\varepsilon\Theta(\varepsilon - \hbar v_\lambda|\boldsymbol{q}|)}{\pi\hbar v_\lambda\sqrt{\varepsilon^2 - \hbar^2 v_\lambda^2|\boldsymbol{q}|^2}} \tag{A18}$$

and

$$\rho^{\mathrm{e}}_\lambda(\varepsilon,q_x) = \frac{a}{L_x}\frac{a^2\varepsilon}{2\pi\hbar^2 v_\lambda^2}\Theta(\varepsilon - \hbar v_\lambda|q_x|) \tag{A19}$$

are density of states for bulk and edge scattering (in which two and one momenta conserved, respectively); here, $\Theta(\varepsilon)$ is the Heaviside step function.

2. Point coupling to a lead

We now derive the collision integral for the system-lead coupling [see Eq. (13)]. We assume a filtered lead with states, $|l\rangle$, and energies $\mathcal{E}_l$, characterized by a composite index, $l = \{k_x,\mathcal{E}_l,\nu\}$, were $\nu = \{\uparrow,\downarrow\}$, and $k_x \in [-\pi/a,\pi/a)$. We take the modes to provide a uniform density of states, independent of k_x and ν, throughout the filter window. We place the filter window centered around the energy $\hbar\Omega/2$ in the original conduction band, with the width of $\hbar\Omega$, i.e. $0 \leqslant \mathcal{E}_l < \hbar\Omega$. The right lead-system Hamiltonian reads

$$\hat{\mathcal{H}}^{\mathrm{R}}_{\mathrm{res}} = \sum_{lp}\left(J^{\mathrm{R}}_{lp}\hat{d}^\dagger_l\hat{c}_p + \mathrm{h.c.}\right) + \sum_l(\mathcal{E}_l - \mu_{\mathrm{res}})\hat{d}^\dagger_l\hat{d}_l, \tag{A20}$$

where the lead system coupling is assumed to have the form $J^{\mathrm{R}}_{lp} = J\delta_{yL_y}\delta_{\nu(p)\nu(l)}\delta_{k_x(p)k_x(l)}$. Here, p is a compact notation to label system states, $p = (k_x,y,\nu)$. The self-energy due to system-lead tunneling is a sum of two terms, which are shown diagrammatically in Fig. 5(b). The Wigner transform of the self-energy due to tunneling of a particle from a bulk state to the right lead reads

$$\Sigma^{\mathrm{b}}_{\mathrm{res,R},\alpha}(\boldsymbol{k},y;\omega) = \frac{2\pi}{\hbar}\sum_{n,l}|J|^2\zeta^{n,\nu(l),\boldsymbol{k}\alpha}_{\mathrm{res,R}}(y)\delta_{k_x,k_x(l)} \times g_l(\omega + n\Omega), \tag{A21}$$

where

$$\zeta^{n,\nu,\boldsymbol{k}\alpha}_{\mathrm{res,R}}(y)=\frac{a}{\pi}\int dk'_y e^{2ik'_y(y-L_y)}\langle\phi^n_{\boldsymbol{k}+k'_y\hat{\boldsymbol{y}}\alpha}|\nu\rangle\langle\nu|\phi^n_{\boldsymbol{k}-k'_y\hat{\boldsymbol{y}}\alpha}\rangle. \tag{A22}$$

Assuming that the Floquet bulk states $\{|\phi^n_{\boldsymbol{k}\alpha}\rangle\}$ only weakly depend on k_y, we approximate $\zeta^{n,\nu,\boldsymbol{k}\alpha}_{\mathrm{res,R}}(y)\approx\delta_{y,Ly}|\langle\phi^n_{\boldsymbol{k}\alpha}|\nu\rangle|^2$. Here $g_l(\omega)=\left(\begin{smallmatrix}g^R_l(\omega) & g^K_l(\omega)\\ 0 & g^A_l(\omega)\end{smallmatrix}\right)$ is the lead's two point Keldysh function, where $g^{R(A)}_l(\omega)=\frac{1}{\omega-\mathcal{E}_l/\hbar\pm i0^+}$, and $g^K_l(\omega)=\tanh\left(\frac{\hbar\omega-\mu_{\mathrm{res}}}{2k_BT}\right)(g^R_l(\omega)-g^A_l(\omega))$. Note that we neglected any off-diagonal terms in the α and α' indices. Those terms vanish in the limit $1/(\Delta\varepsilon\tau_{\mathrm{scat}})\to 0$, where $\Delta\varepsilon$ is of the order of the Floquet gap and τ_{scat} is the average scattering time due to phonon scattering [43]. The self-energy of the right edge-lead self-energy has a similar form,

$$\Sigma^{\mathrm{e}}_{\mathrm{res,R}}(k_x;\omega)=\frac{2\pi}{\hbar}\sum_{n,l}|J|^2\left|\langle\chi^n_{k_x\mathrm{R}}(L_y)|\nu(l)\rangle\right|^2\delta_{k_x,k_x(l)}g_l\times(\omega+n\Omega). \tag{A23}$$

We employ Eq. (A11) to write the collision integral due to tunneling between the right reservoir and the system,

$$\mathcal{I}^{\mathrm{b,res}}_{\boldsymbol{k}\alpha}=\sum_n\mathcal{J}^n_{\boldsymbol{k}\alpha}\left[f_{\mathrm{FD}}\left(\varepsilon^n_\alpha(\boldsymbol{k})-\mu_{\mathrm{res}}\right)-f^{\mathrm{b}}_{\boldsymbol{k}\alpha}\right], \tag{A24a}$$

$$\mathcal{I}^{\mathrm{e,res}}_{k_x\mathrm{R}}=\sum_n\mathcal{J}^n_{k_x\mathrm{R}}\left[f_{\mathrm{FD}}\left(\varepsilon^n_{\mathrm{R}}(k_x)-\mu_{\mathrm{res}}\right)-f^{\mathrm{e}}_{k_x\mathrm{R}}\right], \tag{A24b}$$

where

$$\mathcal{J}^n_{\boldsymbol{k}\alpha}=\frac{2\pi}{\hbar}|J|^2\sum_\nu\zeta^{n,\nu(l),\boldsymbol{k}\alpha}_{\mathrm{res,R}}(y)\mathcal{N}(\varepsilon_\alpha(\boldsymbol{k})+n\hbar\Omega), \tag{A25a}$$

$$\mathcal{J}^n_{k_x\mathrm{R}}=\frac{2\pi}{\hbar}|J|^2\sum_\nu\left|\langle\nu,L_y|\chi^n_{k_x\mathrm{R}}\rangle\right|^2\mathcal{N}(\varepsilon_{\mathrm{R}}(k_x)+n\hbar\Omega), \tag{A25b}$$

and $\mathcal{N}(\varepsilon)$ is a rectangular function around a single Floquet zone, describing the energy filtering window: $\mathcal{N}(\varepsilon)=1$ if $0<\varepsilon<\hbar\Omega$, $\mathcal{N}(\varepsilon)=0$ otherwise.

3. Estimation of the effective parameters in the rate equation

Here we estimate the effective rates in Eq. (5) and analyze how they scale with the system size. We evaluate the effective rates from the rates in the microscopic model [Eqs. (A17)], employing the steady-state distributions, $f^{\mathrm{b}}_{\boldsymbol{k}\alpha}$, $f^{\mathrm{e}}_{k_x\beta}$. We begin with the interband relaxation rate in the bulk, Λ^{inter}. We define the average relaxation rate for particles around minima of the Floquet band as $\overline{\mathcal{W}}^{\mathrm{inter}}=\frac{\int d\boldsymbol{k}d\boldsymbol{k}'W^{\mathrm{bb},\boldsymbol{k}'-}_{s,\boldsymbol{k}+}f^{\mathrm{b}}_{\boldsymbol{k}'+}f^{\mathrm{b}}_{\boldsymbol{k}+}}{\left(\int d\boldsymbol{k}f^{\mathrm{b}}_{\boldsymbol{k}+}\right)^2}$. Then the parameter Λ^{inter} appearing in Eq. (5a), which describes the rate to scatter to any of the hole states in the lower Floquet band, per density of the holes, is given by $\Lambda^{\mathrm{inter}}=L_xL_y\overline{\mathcal{W}}^{\mathrm{inter}}$. At low excitation densities, $a^2n_{\mathrm{b}}\ll 1$, the population is significant near the Floquet band minima, at $\boldsymbol{k}=\boldsymbol{k}_R$. We can then approximate $\overline{\mathcal{W}}^{\mathrm{inter}}\approx W^{\mathrm{bb},\boldsymbol{k}_R-}_{s,\boldsymbol{k}_R+}$. Assuming the matrix elements of the electron-phonon coupling in the active region are of the order g_s, and using the explicit expression for the phonon density of states, at $\boldsymbol{q}=0$ [see Eq. (A18)], we obtain $\overline{\mathcal{W}}^{\mathrm{inter}}\approx g_s^2\frac{2a^3}{\hbar^2v_sL_xL_y}$.

Next, we estimate Γ^{rec} in Eq. (5a). This parameter is associated with the recombination rate for a particle in the upper band. To determine Γ^{rec}, we first compute the rate for a particle with momentum $\boldsymbol{k}$ in the upper band to transition to the lower Floquet by emitting a photon, which we denote by $\mathcal{W}^{\mathrm{rec}}_{\boldsymbol{k}}$. We observe that the momentum transfer in photon-mediated processes with typical energy $\hbar\Omega$, is of the order of $|\boldsymbol{q}|\sim\Omega/v_\ell$, which is small momentum compared to the scale over which the transition rates change. It follows that a state with momentum $\boldsymbol{k}$ can be scattered by a photon to state $\boldsymbol{k}'$, satisfying $|\boldsymbol{k}'-\boldsymbol{k}|\leqslant|\boldsymbol{q}|$ with approximately the same rate. Since there are approximately $\sim\pi|\boldsymbol{q}|^2/(\frac{4\pi^2}{L_xL_y})\approx\frac{L_xL_y}{4\pi}\frac{\Omega^2}{v_\ell^2}$ such states, we can approximate $\mathcal{W}^{\mathrm{rec}}_{\boldsymbol{k}}\approx\frac{L_xL_y}{4\pi}\frac{\Omega^2}{v_\ell^2}W^{\mathrm{bb},\boldsymbol{k}+}_{\ell,\boldsymbol{k}-}$. The parameter Γ^{rec} is then defined as $\Gamma^{\mathrm{rec}}=\frac{A_{\mathcal{R}}}{(2\pi)^2}\overline{\mathcal{W}}^{\mathrm{rec}}$, where $\overline{\mathcal{W}}^{\mathrm{rec}}$ is the average value of $\mathcal{W}^{\mathrm{rec}}_{\boldsymbol{k}}$ within the resonance curve, and $A_{\mathcal{R}}$ is the momentum-space area inside this curve (see the inset in Fig. 1). Assuming that the matrix elements of the electron-photon coupling in the active region are of the order g_ℓ, and using the explicit expression for the photon density of states, we obtain $\overline{\mathcal{W}}^{\mathrm{rec}}\approx g_\ell^2\frac{a^3\Omega^2}{2\pi\hbar^2v_\ell^3}$. With these approximate expressions for Γ^{rec} and Λ^{inter} at hand, we are at the position to write the approximate expression for $\kappa=\frac{\Gamma^{\mathrm{rec}}}{\Lambda^{\mathrm{inter}}}$, that reads $\kappa\approx\frac{A_{\mathcal{R}}\Omega^2v_sg_s^2}{8\pi^3v_\ell^3g_s^2}$.

Next, we deal with the rate equation for the excited particles on the edge, Eq. (5b). As in the main text, we define n_{e} as the occupation of state with $k_x>0$. To estimate the bulk-to-edge and edge-to-bulk processes let us define the average rate to scatter from the minima of the upper band to an edge state labeled by k_x (we denote this average rate by $\overline{\mathcal{W}}^{\mathrm{b}\to\mathrm{e}}_{k_x}$). Likewise, we define the average rate to scatter from the edge to a maximum of the lower band (which we denote by $\overline{\mathcal{W}}^{\mathrm{e}\to\mathrm{b}}$). The second process occurs essentially near $k_x=0$, where most of the excitations accumulate. We define these rates as $\overline{\mathcal{W}}^{\mathrm{b}\to\mathrm{e}}_{k_x}=\frac{\int d\boldsymbol{k}W^{\mathrm{be},k_x\mathrm{R}}_{s,\boldsymbol{k}+}f^{\mathrm{b}}_{\boldsymbol{k}+}}{\int d\boldsymbol{k}f^{\mathrm{b}}_{\boldsymbol{k}+}}$, and $\overline{\mathcal{W}}^{\mathrm{e}\to\mathrm{b}}=\frac{\int d\boldsymbol{k}\int_0^{k_R}dk_xW^{\mathrm{eb},k_x\mathrm{R}}_{s,\boldsymbol{k}+}f^{\mathrm{b}}_{\boldsymbol{k}+}f^{\mathrm{e}}_{k_x\mathrm{R}}}{\int d\boldsymbol{k}\int_0^{k_R}dk_xf^{\mathrm{b}}_{\boldsymbol{k}+}f^{\mathrm{e}}_{k_x\mathrm{R}}}$, respectively. The parameter $\gamma^{\mathrm{b}\to\mathrm{e}}$ in Eq. (5b) describes the scattering rate from the bulk to the edge per bulk density, per unit length. This process occurs essentially uniformly along edge states with $\varepsilon>0$, and can be approximated as $\gamma^{\mathrm{b}\to\mathrm{e}}\approx L_xL_y\int_0^{k_R}\frac{dk_x}{2\pi}\overline{\mathcal{W}}^{\mathrm{b}\to\mathrm{e}}_{k_x}$. Similarly, the edge-to-bulk rate per bulk density is given by $\Lambda^{\mathrm{e}\to\mathrm{b}}\approx L_xL_y\overline{\mathcal{W}}^{\mathrm{e}\to\mathrm{b}}$. Finally, the parameter $\gamma^{\mathrm{e}\to\mathrm{e}}$ can be estimated as $\gamma^{\mathrm{e}\to\mathrm{e}}\approx L_x\overline{\mathcal{W}}^{\mathrm{e}\to\mathrm{e}}$, where $\overline{\mathcal{W}}^{\mathrm{e}\to\mathrm{e}}=\frac{\int_0^{k_R}dk_xdk'_xW^{\mathrm{ee},-k'_x\mathrm{R}}_{s,k_x\mathrm{R}}f^{\mathrm{e}}_{k_x\mathrm{R}}f^{\mathrm{e}}_{k'_x\mathrm{R}}}{\left(\int_0^{k_R}dk_xf^{\mathrm{e}}_{k_x\mathrm{R}}\right)^2}$.

APPENDIX B: SPATIAL STRUCTURE OF THE STEADY STATE

Here we analyze the spatial structure of the bulk density in the steady state [see Fig. 3(a)] using a reaction-diffusion equation. We begin with the reaction-diffusion equation for

the density of the bulk excitations in the steady state [43],

$$D\partial_y^2 n_{\rm b}(y) = \Gamma^{\rm rec} - \Lambda^{\rm inter} n_{\rm b}^2(y). \tag{B1}$$

Here, D is the diffusion constant, given by $D \approx \bar{v}^2\tau$, where $\bar{v}$ is a typical velocity of the excited carriers and τ is the scattering time (dominated by phonon scattering). We solve this equation with boundary conditions at the edges of the system, such that the bulk current normal to the edges equals the rate of scattering into the edge states. For example, at the right edge of the system ($y = L_y$), the bulk current is given by $D\partial_y n_{\rm b}(L_y)$ and we set $D\partial_y n_{\rm b}(L_y) = -\gamma^{\rm b\to e} n_{\rm b}(L_y) + \Lambda^{\rm e\to b} n_{\rm b}(L_y) n_{\rm e}$. Assuming that the density of the bulk excitations is not strongly affected by the presence of the edge, we linearize Eq. (B1) around the bulk value, writing $\Delta n_{\rm b}(y) = n_{\rm b}(y) - n_{\rm b}^0$, where $n_{\rm b}^0 = n_{\rm b}(L_y/2)$. The diffusion equation then reads, $\partial_y^2 \Delta n_{\rm b}(y) = \Delta n_{\rm b}(y)/\xi^2$ where $\xi = \sqrt{Dn_{\rm b}^0/(2\Gamma^{\rm rec})}$. Additionally, we neglect the second term in the equation determining the boundary condition for the current, which is proportional to $\Lambda^{\rm e\to b}$, since at low excitation density, the first term in this equation dominates [see the discussion above Eq. (7)]. Solving Eq. (B1) with the above boundary conditions we arrive at the expression for $\Delta\tilde{n}_{\rm b}(y) = \frac{\Delta n_{\rm b}(y)}{n_{\rm b}^0}$,

$$\Delta\tilde{n}_{\rm b}(y) = -\frac{\cosh((y - L_y/2)/\xi)}{\cosh(L_y/2\xi) + \frac{2\Gamma^{\rm rec}\xi}{\gamma^{\rm b\to e} n_{\rm b}^0}\sinh(L_y/2\xi)}. \tag{B2}$$

Taking the limit $L_y \gg \xi \gg a$, we obtain

$$\Delta\tilde{n}_{\rm b}(0) = -\frac{\gamma^{\rm b\to e} n_{\rm b}^0}{2\Gamma^{\rm rec}\xi}. \tag{B3}$$

For our parameters (see Table I), the estimate (B3) yields $\Delta\tilde{n}_{\rm b}(0) \sim 10^{-3}$, which is in a good agreement with our results [see Fig. 3(a)].

The estimate in Eq. (B3) can be also obtained from Eq. (5a). We first write $n_{\rm b} = n_{\rm b}^0 + \delta n_{\rm b}$, where $n_{\rm b}^0$ is the solution absent the bulk-edge scattering, and expand Eq. (5a) to first order in $\delta n_{\rm b}$. We then assume that the excess number of particles excited due to edge-to-bulk scattering, $\delta N_{\rm b} = \delta n_{\rm b} L_x L_y$, accumulate only on a strip of width ξ near each edge. The excess density in this strip is then given by Eq. (B3).

APPENDIX C: DETAILS OF THE NUMERICAL SIMULATIONS

Here we summarize the details of the numerical simulations. We discretize the phase space using a grid of $N_{k_x} \times N_{k_y} = 50 \times 50$ sites in momentum space, and $N_y = 11$ sites in real space along the y direction. For a physical system size of L_y, we define θ to be the sampling ratio of k points, whereby $L_y = a\theta N_{k_y}$ (e.g., $\theta = 2$ means that we take every second k point). Furthermore, the discretization step in the y direction is given by $\Delta y = L_y/N_y = a\theta N_{k_y}/N_y$.

The discrete version of the steady-state Boltzmann equation [see Eq. (9)] reads

$$v_{y,\alpha}(\boldsymbol{k}) \frac{f_{\boldsymbol{k}\alpha}^{\rm b}(j+1) - f_{\boldsymbol{k}\alpha}^{\rm b}(j)}{a\theta N_{k_y}/N_y} = \mathcal{I}_{\boldsymbol{k}\alpha}^{\rm tot}(j), \tag{C1}$$

where j is a discrete index indicating the position in the y direction, i.e., $y = j\Delta y$. Here we denote by $\mathcal{I}_{\boldsymbol{k}\alpha}^{\rm tot}(j)$ the total contribution from the bulk and the edge collision integrals. We now multiply Eq. (C1) by θ and Ω^{-1} to arrive at the dimensionless expression

$$\frac{v_{y,\alpha}(\boldsymbol{k})}{\Omega a} \frac{f_{\boldsymbol{k}\alpha}^{\rm b}(j+1) - f_{\boldsymbol{k}\alpha}^{\rm b}(j)}{N_{k_y}/N_y} = \frac{\theta\mathcal{I}_{\boldsymbol{k}\alpha}^{\rm tot}(j)}{\Omega}. \tag{C2}$$

We fix $\sqrt{\theta} g_s$ on the value that ensures that the step size $\Delta y = L_y/N_y$ is on the order of the healing length ξ, evaluated below [see also Fig. 3(a)].

Due to the discretization of real space in the y direction, in the bulk-edge collision terms $\mathcal{I}_{\boldsymbol{k}\alpha}^{\rm be}(j)$ we replace $\delta_{\alpha,0}$ by $\frac{a}{\Delta y}\delta_{j,0}$ and δ_{α,L_y} with $\frac{a}{\Delta y}\delta_{j,11}$, see Eqs. (A13b), (A17b), and (A17d). The prefactor, $a/\Delta y$, makes sure that the integrals of the new and the old δ functions are the same. Notice that Eq. (C2) is *not invariant* under the rescaling, $\theta \to \lambda\theta$, $g_s \to g_s/\sqrt{\lambda}$, $g_\ell \to g_s/\sqrt{\lambda}$ due to the $a/\Delta y$ prefactor in the bulk-to-edge collision integral. Therefore both $L_y = a\theta N_{k_y}$ as well as g_s and $\kappa \sim g_\ell^2/g_s^2$ have to specified when specifying the parameters of the simulation. We find the steady-state solution to the Boltzmann equation [Eq. (9)] employing the Newton-Raphson method, for the parameters in Table I.

To find the physical length and scattering rates in the system, we fix $\Omega = 100$ THz, and $a = 5.6$ Å. This gives $\tau_{\rm he} \approx 0.1$ ps in agreement with literature 61], and $L = 56$ μm. Here, we employed the relation $g_s \approx \hbar\sqrt{\frac{v_s}{2a\tau_{\rm he}}}$.

APPENDIX D: FITS OF THE STEADY STATES TO FERMI-DIRAC AND QUASI-FERMI-DIRAC DISTRIBUTIONS

In this section we discuss the fit of the bulk distribution to a distribution described by separate Fermi functions for electrons and holes, and the fit of the edge to a quasi-Fermi-Dirac distribution (for a system not coupled to leads).

1. Distribution of the bulk

The steady state of the bulk is described by two separate Fermi-Dirac distributions, one for electrons in the upper Floquet band (+), and one for electrons in the lower Floquet band (−). The chemical potentials of these distributions, μ_+ and μ_-, are related by particle hole symmetry, $f_{\boldsymbol{k}+}^{\rm b} = 1 - f_{\boldsymbol{k}-}^{\rm b}$, which implies $\mu_+ = -\mu_- \equiv \mu_{\rm b}$. Note that for any $\kappa > 0$, the chemical potentials are shifted away from $\varepsilon = 0$. Particle hole symmetry further implies that the effective temperatures, $T_{\rm b}$, of the distributions in the both bands must be equal. Figure 6(a) displays the least mean square fit of $f_{\boldsymbol{k}+}^{\rm b}$ to the Fermi-Dirac distribution. The effective temperature increases as κ increases (hence the temperature increases with the excitation density). We also measured the goodness of the fits of the bulk distribution to Fermi-Dirac function and the edge to quasi-Fermi-Dirac distribution [effective parameters $T_{\rm e}$ and δ of the quasi-Fermi-Dirac distribution appear in the inset to Fig. 3(c)]. We define the parameters $\mathcal{Q}_{\rm b}$ and $\mathcal{Q}_{\rm e}$, for the bulk

TABLE I. A list of the parameters used in the numerical simulations, and physical quantities corresponding to these simulation parameters.

Simulation parameters							Physical parameters	
A	M	B	V_0	$\sqrt{\theta}g_s$	θ	N_y	Ω	a
$0.2\hbar\Omega$	$0.2\hbar\Omega$	$-0.09\hbar\Omega$	$0.2\hbar\Omega$	$1\hbar\Omega$	2000	11	100 THz	5.6 Å
v_s	v_ℓ	ω_D	k_BT	J	N_{k_x}	N_{k_y}	τ_{he}	L_y
$0.0092a\Omega$	$1a\Omega$	0.15Ω	0	$0.2\hbar\Omega$	50	50	0.1 ps	56 μm

and the edge distributions, as

$$\mathcal{Q}_b \equiv 1 - \frac{a^2}{L_x L_y}\sum_{\boldsymbol{k}} \frac{\left|f^b_{\boldsymbol{k}+} - f_{FD}(T_b,\mu_b)\right|}{\max\left\{f^b_{\boldsymbol{k}+}\right\}},$$
$$\mathcal{Q}_e \equiv 1 - \frac{a}{L_x}\sum_{k_x}\left|f^e_{k_xR} - f_{QFD}(T_e,\delta)\right|. \quad \text{(D1)}$$

The goodness of fit parameters are shown in Fig. 6(b). It shows an improvement of the fit as κ decreases. A similar effect was found in Ref [43].

2. Distribution of the edge

In this section, we estimate how the parameters δ and T_e of the quasi-Fermi-Dirac distribution, f_{QFD}, scale with κ using a rate equation approach. First, we observe that the majority of the excitations of the edge states are concentrated near $k_x = 0$ point. A small fraction of the excitations are distributed approximately uniformly along the edge. We choose an arbitrary point k_S, such that the majority of the excitations are within $0 < k_x < k_S$. At small κ, the density $n_\delta \equiv \int_{k_S}^{k_R}\frac{dk_x}{2\pi} f^e_{k_xR}$ is significantly smaller than $n_T \equiv n_e - n_\delta \approx n_e$, hence

$$n_T \sim \kappa^{\frac{1}{4}}. \quad \text{(D2)}$$

The parameters δ and T_e can be expressed in terms of n_δ and n_T. Using $f_{QFD}(T_e,\delta)$ for $f^e_{k_xR}$ in the definitions of n_δ and n_T, and assuming a constant edge velocity, v_e, we obtain for $\delta \ll 1$,

$$n_T \approx \frac{k_B T_e \ln(2)}{\pi a \Delta_1}, \qquad n_\delta \approx \frac{k_R - k_S}{4\pi}\delta. \quad \text{(D3)}$$

Now we are at the position to write the rate equation for n_δ. The difference between this equation and Eq. (5b) is in an additional rate to scatter from the interval $k_S < k_x < k_R$ to the interval of $0 < k_x < k_S$. Since for small κ the interval $0 < k_x < k_S$ (as the entire upper half of the edge) is almost empty ($an_T \ll 1$), the term responsible for this scattering process in the rate equation is proportional to $\sim R^{e\to e}n_\delta(1 - an_T) \approx R^{e\to e}n_\delta$. Other scattering processes of n_δ are similar to scattering processes of n_e [see Eq. (5b)], albeit with different effective rate parameters. The rate equation for n_δ then reads

$$\dot{n}_\delta = \tilde{\gamma}^{b\to e}n_b - \tilde{\Lambda}^{e\to b}n_b n_\delta - \tilde{\gamma}^{e\to e}n_\delta^2 - R^{e\to e}n_\delta. \quad \text{(D4)}$$

Note that the term $R^{e\to e}$ did not appear in Eq. (5b), which was a rate equation for the full edge state excitation density n_e; in comparison, Eq. (D4) is rate equation for excitations in the interval $k_S < k_x < k_R$ only. In the limit of small κ, the terms proportional to $\tilde{\Lambda}^{e\to b}$ and $\tilde{\gamma}^{e\to e}$ can be neglected, yielding $n_\delta = \frac{\tilde{\gamma}^{b\to e}}{R^{e\to e}}n_b$. Hence n_δ scales as

$$n_\delta \sim \kappa^{\frac{1}{2}}. \quad \text{(D5)}$$

Finally, we combine the relations between T_e and δ and n_T and n_δ [see Eq. (D3)], with the scalings of n_T and n_δ with κ [see Eqs. (D2) and (D4)] to obtain

$$T_e \sim \kappa^{\frac{1}{4}}, \qquad \delta \sim \kappa^{\frac{1}{2}}. \quad \text{(D6)}$$

Our numerical results confirm the prediction in the Eq. (D6) [see inset in Fig. 3(c)].

APPENDIX E: CONDUCTANCE IN A TWO-PROBE SETUP

In this section, we derive the conductance in the two-terminal setup [see Fig. 2(b)]. The left and the right leads with chemical potentials $\mu^L_{res} = eV$ and $\mu^R_{res} = 0$ are connected at

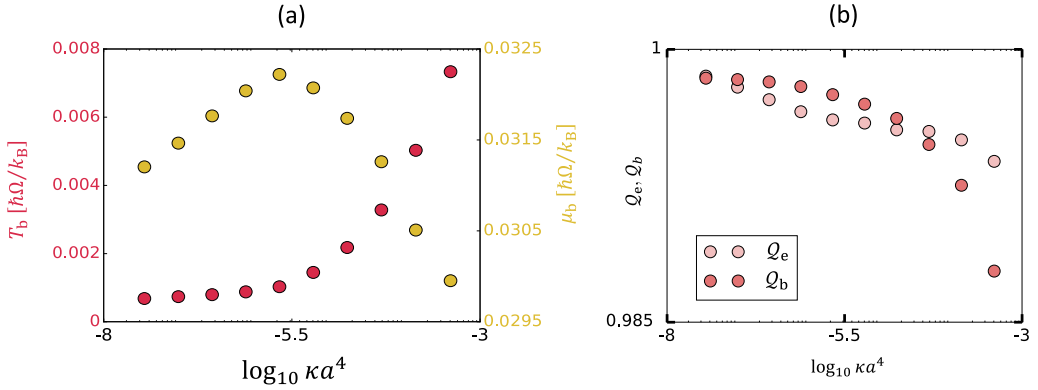

FIG. 6. (a) Effective parameters of the Fermi-Dirac distribution that fit the upper Floquet band steady state. (b) The parameters determining the goodness of the fits to Fermi-Dirac distribution in the bulk and quasi-Fermi-Dirac distribution of the edge, see the definitions in Eq. (D1). Effective parameters T_e and δ of the quasi-Fermi-Dirac distribution that fit the distribution of the edge appear in the inset to Fig. 3(c).

$y = 0$ and L_y, respectively. The total current in this geometry has two contributions from the bulk and the edge currents. The bulk contribution is computed from Ohm's law, with a conductivity tensor, which we compute in Sec. E 1. The conductivity tensor has both diagonal and off-diagonal components arising from the Berry curvature of the Floquet-Bloch bands. The edge current is derived in Sec. E 2 from the continuity equation, taking into account scattering processes discussed in the main text.

1. Bulk contribution to the conductance

We first derive the conductivity tensor for the bulk of a FTI. The conductivity tensor has both longitudinal, $\sigma^{\rm b}_{yy}$, and transversal, $\sigma^{\rm b}_{xy}$, contributions. To find them in the clean limit, we write the Boltzmann equation for the bulk [see Eq. (9)] in the relaxation time approximation. To find the response to external field, we include the coupling of the electric field to momentum gradients, $\partial_t f_{\boldsymbol{k}} \sim (e/\hbar)\boldsymbol{E}\cdot\partial_{\boldsymbol{k}} f_{\boldsymbol{k}}$. In the steady state, the Boltzmann equation for the electrons and the holes in the relaxation time approximation with a relaxation rate $\tau_{\boldsymbol{k}\pm}$ reads

$$\boldsymbol{v}_+(\boldsymbol{k})\cdot\partial_{\boldsymbol{r}} f^{\rm b}_{\boldsymbol{k}+}(\boldsymbol{r}) - (e/\hbar)\boldsymbol{E}\cdot\partial_{\boldsymbol{k}} f^{\rm b}_{\boldsymbol{k}+}(\boldsymbol{r}) = -\delta f^{\rm b}_{\boldsymbol{k}+}(\boldsymbol{r})/\tau_{\boldsymbol{k}+}, \tag{E1a}$$

$$\boldsymbol{v}_-(\boldsymbol{k})\cdot\partial_{\boldsymbol{r}} \bar{f}^{\rm b}_{\boldsymbol{k}-}(\boldsymbol{r}) - (e/\hbar)\boldsymbol{E}\cdot\partial_{\boldsymbol{k}} \bar{f}^{\rm b}_{\boldsymbol{k}-}(\boldsymbol{r}) = -\delta \bar{f}^{\rm b}_{\boldsymbol{k}-}(\boldsymbol{r})/\tau_{\boldsymbol{k}-}. \tag{E1b}$$

Here, $\delta f^{\rm b}_{\boldsymbol{k}+}(\boldsymbol{r}) = f^{\rm b}_{\boldsymbol{k}+}(\boldsymbol{r}) - f^{\rm b,0}_{\boldsymbol{k}+}(\boldsymbol{r})$ is the deviation from the "local steady-state" distribution, $f^{\rm b,0}_{\boldsymbol{k}\alpha}$, satisfying $\mathcal{I}^{\rm bb}_{\boldsymbol{k}\alpha}\{f^{\rm b,0}_{\boldsymbol{k}\alpha}\} = 0$. The velocity vector contains both the band velocity and the anomalous velocity components, namely $\boldsymbol{v}_\alpha(\boldsymbol{k}) = \hbar^{-1}[\partial_{\boldsymbol{k}}\varepsilon_\alpha(\boldsymbol{k}) + e\boldsymbol{E}\times\boldsymbol{\mathcal{F}}_{\alpha\boldsymbol{k}}]$, where $\boldsymbol{\mathcal{F}}_{\alpha\boldsymbol{k}}$ is the Berry curvature averaged over one period, given by $\boldsymbol{\mathcal{F}}_{\alpha\boldsymbol{k}} = \sum_n \nabla\times\boldsymbol{\mathcal{A}}^n_{\alpha\boldsymbol{k}}$, where $\boldsymbol{\mathcal{A}}^n_{\alpha\boldsymbol{k}} = \langle\phi^n_{\boldsymbol{k}\alpha}|i\nabla|\phi^n_{\boldsymbol{k}\alpha}\rangle$. The solution to Eqs. (E1) to leading order in $\delta f^{\rm b}$ and derivatives of $f^{\rm b}$ reads

$$\begin{aligned} f^{\rm b}_{\boldsymbol{k}+}(\boldsymbol{r}) = {} & f^{\rm b,0}_{\boldsymbol{k}+}(\boldsymbol{r}) - \tau_{\boldsymbol{k}+}\boldsymbol{v}_+(\boldsymbol{k})\cdot\partial_{\boldsymbol{r}} f^{\rm b}_{\boldsymbol{k}+}(\boldsymbol{r}) \\ & + \tau_{\boldsymbol{k}+}(e/\hbar)\boldsymbol{E}\cdot\partial_{\boldsymbol{k}} f^{\rm b}_{\boldsymbol{k}+}(\boldsymbol{r}), \end{aligned} \tag{E2a}$$

$$\begin{aligned} \bar{f}^{\rm b}_{\boldsymbol{k}-}(\boldsymbol{r}) = {} & \bar{f}^{\rm b,0}_{\boldsymbol{k}-}(\boldsymbol{r}) - \tau_{\boldsymbol{k}-}\boldsymbol{v}_-(\boldsymbol{k})\cdot\partial_{\boldsymbol{r}} \bar{f}^{\rm b}_{\boldsymbol{k}-}(\boldsymbol{r}) \\ & + \tau_{\boldsymbol{k}-}(e/\hbar)\boldsymbol{E}\cdot\partial_{\boldsymbol{k}} \bar{f}^{\rm b}_{\boldsymbol{k}-}(\boldsymbol{r}). \end{aligned} \tag{E2b}$$

With this form for the electron and hole distributions, we can find the current density, given as

$$\boldsymbol{J} = \sum_{\alpha=\pm}\int \frac{d^2\boldsymbol{k}}{(2\pi)^2} e\boldsymbol{v}_\alpha(\boldsymbol{k}) f^{\rm b,0}_{\boldsymbol{k}\alpha}. \tag{E3}$$

The conductivity tensor is defined by $\sigma^{\rm b}_{ij} = \frac{\partial J_i}{\partial E_j}$. Assuming an isotropic system, it is enough to find only two components, $\sigma^{\rm b}_{yy}$ and $\sigma^{\rm b}_{xy}$. In a realistic system, the relaxation rates have contribution both from phonons and disorder scattering. The total longitudinal conductivity from both contributions is found from Matthiessen's rule, $1/\sigma^{\rm b}_{yy} = 1/\sigma^{\rm b}_{{\rm ph},yy} + 1/\sigma^{\rm b}_{{\rm imp},yy}$. Note that although the phonon bath is at zero temperature, the contribution of phonons to the scattering rate does not vanish in the steady state of the system. The expression for phonon contribution to longitudinal component of the conductivity is given by

$$\sigma^{\rm b}_{{\rm ph},yy} = 2\frac{e^2}{h}\int d^2\boldsymbol{k}\big(h^{-1}\partial_{k_y}\varepsilon_+(\boldsymbol{k})\cdot\partial_{k_y} f^{\rm b,0}_{\boldsymbol{k}_+}\big)\tau^{\rm ph}_{\boldsymbol{k}_+}, \tag{E4}$$

where the phonon relaxation time is approximated by $1/\tau^{\rm ph}_{\boldsymbol{k}\alpha} \approx \frac{\delta\mathcal{I}^{\rm bb}_{\boldsymbol{k}\alpha}}{\delta f^{\rm b}_{\boldsymbol{k}\alpha}}\big|_{f^{\rm b,0}_{\boldsymbol{k}\alpha}}$ with $\mathcal{I}^{\rm bb}_{\boldsymbol{k}\alpha}$ given by Eq. (A13a). Here we assumed particle hole symmetry; the label "ph" denotes the contribution from phonon scattering. The transversal component reads

$$\sigma^{\rm b}_{xy} = \frac{e^2}{h}\frac{1}{2\pi}\sum_{\alpha=\pm}\int d^2\boldsymbol{k}(\hat{\boldsymbol{z}}\cdot\boldsymbol{\mathcal{F}}_{\boldsymbol{k}\alpha}) f^{\rm b,0}_{\boldsymbol{k}\alpha}. \tag{E5}$$

We approximate the impurity contribution to longitudinal conductivity by $\sigma^{\rm b}_{{\rm imp},yy} = 2en_{\rm b}\mu_{\rm imp}$, where $\mu_{\rm imp}$ is the typical mobility due to impurity scattering. Figure 7 shows the longitudinal and the transverse conductivities versus κa^4 for $\mu_{\rm imp} = 1000\,{\rm cm}^2/({\rm V\,sec})$, where the phonon contribution [see Eqs. (E4) and (E5)] was computed in the steady state of the system.

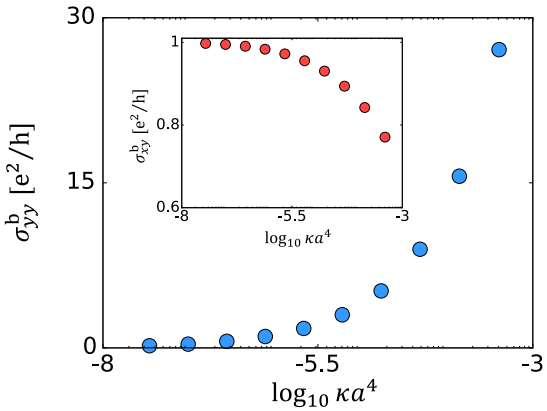

FIG. 7. The longitudinal ($\sigma^{\rm b}_{yy}$) and the transversal ($\sigma^{\rm b}_{xy}$) components of the bulk conductivity tensor vs κa^4. The longitudinal component contains both the phonon contribution and the impurity contribution, for the typical value $\mu_{\rm imp} = 1000\ {\rm cm}^2/({\rm V\,sec})$. The transversal component (inset) includes only the intrinsic contribution.

In principle, the scattering from impurities may affect the transverse component as well due to skew scattering and side jump processes [64]. Here we do not consider these effects, focusing on the intrinsic contribution alone. A full analysis of skew scattering and side jumps in the Floquet system is an interesting subject for future work.

Now, we are ready to estimate the current in the two-probe geometry. The current in the bulk can be computed from the electric potential, $V(x,y)$, by Ohm's law, $J_i = \sigma^{\rm b}_{ij}\partial_i V$. To find $V(x,y)$, one needs to solve the Laplace equation, $\nabla^2 V = 0$, with appropriate boundary conditions. Along the open edges [edges along the y direction in Fig. 2(b)], we require the currents to be zero in the normal to the edges direction, $\hat{\boldsymbol{n}}$, i.e., $\hat{n}_i\sigma^{\rm b}_{ij}\partial_i V = 0$. Near the leads, we apply Dirichlet boundary conditions, i.e., $V(x,0) = V$, and $V(x,L_y) = 0$. The current distribution in such a geometry is found in Ref. [76], which showed that the Hall contribution to the total current vanishes,

leaving us with the expression for the conductance, $G^{\mathrm{b}} = (L_x/L_y)\sigma^{\mathrm{b}}_{yy}$.

2. Edge contribution to the conductance

To find the contribution to the conductance from the edges along the y direction in Fig. 2(b), we write two continuity equations for the edges going to the left and the right. These continuity equations are similar to Eq. (5b), albeit with two changes: (i) the excitation density on the edge may depend on the distance from the lead, due to different chemical potentials of the right and the left leads, and (ii) a shift of the chemical potential from $\varepsilon = 0$ breaks the particle hole symmetry, leading to a different density of electrons (Δn_{e}) and holes (Δh_{e}) on the edge. The densities of electrons and holes are evaluated as integrals over the edge distribution shifted by the chemical potential, μ_{e}, i.e., $\Delta n_{\mathrm{e}} = \int_0^{k_R} \frac{dk_y}{2\pi} f^{\mathrm{e}}_{k_y}(\mu_{\mathrm{e}})$, and $\Delta h_{\mathrm{e}} = \int_{-k_R}^{0} \frac{dk_y}{2\pi}(1 - f^{\mathrm{e}}_{k_y}(\mu_{\mathrm{e}}))$, where we replace $f^{\mathrm{e}}_{k_y}(\mu_{\mathrm{e}})$ by the "quasi-Fermi-Dirac" distribution, $f^{\mathrm{e}}_{k_y}(\mu_{\mathrm{e}}) \approx f_{\mathrm{QFD}}(\hbar v_{\mathrm{e}} k_y - \mu_{\mathrm{e}}) = (1-\delta) f_{\mathrm{FD}}(\hbar v_{\mathrm{e}} k_y - \mu_{\mathrm{e}}) + \frac{1}{2}\delta$. Then to leading order in μ_{e}, we obtain

$$\Delta n_{\mathrm{e}} \approx n_{\mathrm{e}} + \frac{\mu_{\mathrm{e}}}{4\pi\hbar v_{\mathrm{e}}}, \qquad \Delta h_{\mathrm{e}} \approx n_{\mathrm{e}} - \frac{\mu_{\mathrm{e}}}{4\pi\hbar v_{\mathrm{e}}}, \tag{E6}$$

where n_{e} is the steady-state solution far away from the leads, as in Eq. (7). To capture the spatial dependence of the densities, we include a new gradient term. The continuity equation for the right edge in the steady state then reads

$$\Delta\dot{n}_{\mathrm{e}} + v_{\mathrm{e}}\partial_y \Delta n_{\mathrm{e}} = \gamma^{\mathrm{b}\to\mathrm{e}} n_{\mathrm{b}} - \Lambda^{\mathrm{e}\to\mathrm{b}} n_{\mathrm{b}} \Delta n_{\mathrm{e}} - \gamma^{\mathrm{e}\to\mathrm{e}} \Delta n_{\mathrm{e}} \Delta h_{\mathrm{e}}, \tag{E7}$$

where we have approximated the edge velocity by a constant, v_{e}. As in Eq. (5b), the terms on the right-hand side of Eq. (E7) correspond to edge-to-edge and edge-to-bulk relaxation and recombination terms. We then expand Eq. (E7) to leading order in μ_{e}, employing Eq. (E6), and take the steady-state limit $\Delta\dot{n}_{\mathrm{e}} = 0$, to obtain

$$v_{\mathrm{e}}\partial_y \mu_{\mathrm{e}} = -\mu_{\mathrm{e}}/\tau_{\mathrm{e}} + \mathcal{O}\big(\mu_{\mathrm{e}}^2\big), \tag{E8}$$

where

$$\tau_{\mathrm{e}} = (\Lambda^{\mathrm{e}\to\mathrm{b}} n_{\mathrm{b}})^{-1}. \tag{E9}$$

Notice that the leading contribution of a term proportional to $\gamma^{\mathrm{e}\to\mathrm{e}}$ in Eq. (E7) is second order in μ_{e}. We solve Eq. (E8) with the boundary condition near the left lead ($y = 0$), $\mu_{\mathrm{e}} = eV$, to obtain $\mu_{\mathrm{e}}(y) = eVe^{-y/v_{\mathrm{e}}\tau_{\mathrm{e}}}$. The edge contribution to the conductance is then found from $G^{\mathrm{e}} = \frac{\partial I}{\partial V}|_{y=L_y} = \frac{\partial}{\partial V}\int_{-k_R}^{k_R} \frac{dk_y}{2\pi} e v_{\mathrm{e}} f_{\mathrm{QFD}}[\hbar v_{\mathrm{e}} k_y - \mu_{\mathrm{e}}(L_y)]$, yielding $G^{\mathrm{e}} = (e^2/h)(1-\delta)e^{-L_y/v_{\mathrm{e}}\tau_{\mathrm{e}}}$.

To check that τ_{e} is indeed given by Eq. (E9) in the limit of small μ_{e}, we derive an expression for τ_{e} from the Boltzmann equation, in the steady state. We then use this expression to compute numerically the lifetime of electrons on the edge in our model [see inset in Fig. 4(b)]. To obtain τ_{e}, we linearize Eq. (A12b) around the steady state at half-filling (i.e., taking linear order in μ_{e}), in the absence of leads, $f^{\mathrm{e}}_{k_x\mathrm{R}} = f^{\mathrm{e},0}_{k_x\mathrm{R}} + \delta f^{\mathrm{e}}_{k_x\mathrm{R}}$, where $\delta f^{\mathrm{e}}_{k_x\mathrm{R}} = \frac{\partial f^{\mathrm{e}}_{k_x\mathrm{R}}}{\partial \mu_{\mathrm{e}}}|_{\mu_{\mathrm{e}}=0}\mu_{\mathrm{e}}$. Then

$$\begin{aligned}\delta\dot{f}^{\mathrm{e}}_{k_x\mathrm{R}} = &\sum_{\boldsymbol{k}'\alpha'}\big[W^{\mathrm{be},k_x\mathrm{R}}_{\boldsymbol{k}'\alpha'} f^{\mathrm{b},0}_{\boldsymbol{k}'\alpha'} \bar{f}^{\mathrm{e}}_{k_x\mathrm{R}} - W^{\mathrm{eb},\boldsymbol{k}'\alpha'}_{k_x\mathrm{R}} f^{\mathrm{e}}_{k_x\mathrm{R}} \bar{f}^{\mathrm{b},0}_{\boldsymbol{k}'\alpha'}\big] \\ &+ \sum_{-k_R<k'_x<k_R}\big[W^{\mathrm{ee},k_x\mathrm{R}}_{k'_x\mathrm{R}} f^{\mathrm{e}}_{k'_x\mathrm{R}} \bar{f}^{\mathrm{e}}_{k_x\mathrm{R}} - W^{\mathrm{ee},k'_x\mathrm{R}}_{k_x\mathrm{R}} f^{\mathrm{e}}_{k_x\mathrm{R}} \bar{f}^{\mathrm{e}}_{k'_x\mathrm{R}}\big],\end{aligned} \tag{E10}$$

where $\bar{f} = 1 - f$. Keeping only linear terms in δf, we obtain

$$\begin{aligned}\delta\dot{f}^{\mathrm{e}}_{k_x\mathrm{R}} = &-\sum_{\boldsymbol{k}'\alpha'}\big[W^{\mathrm{be},k_x\mathrm{R}}_{\boldsymbol{k}'\alpha'} f^{\mathrm{b},0}_{\boldsymbol{k}'\alpha'} + W^{\mathrm{eb},\boldsymbol{k}'\alpha'}_{k_x\mathrm{R}} \bar{f}^{\mathrm{b},0}_{\boldsymbol{k}'\alpha'}\big]\delta f^{\mathrm{e}}_{k_x\mathrm{R}} \\ &- \sum_{-k_R<k'_x<k_R}\Big[W^{\mathrm{ee},k_x\mathrm{R}}_{k'_x\mathrm{R}} f^{\mathrm{e},0}_{k'_x\mathrm{R}} + W^{\mathrm{ee},k'_x\mathrm{R}}_{k_x\mathrm{R}} \bar{f}^{\mathrm{e},0}_{k'_x\mathrm{R}}\Big]\delta f^{\mathrm{e}}_{k_x\mathrm{R}} \\ &+ \sum_{-k_R<k'_x<k_R}\Big[W^{\mathrm{ee},k_x\mathrm{R}}_{k'_x\mathrm{R}} \bar{f}^{\mathrm{e},0}_{k_x\mathrm{R}} + W^{\mathrm{ee},k'_x\mathrm{R}}_{k_x\mathrm{R}} f^{\mathrm{e},0}_{k_x\mathrm{R}}\Big]\delta f^{\mathrm{e}}_{k'_x\mathrm{R}} \\ &+ \mathcal{O}(\delta f^2).\end{aligned} \tag{E11}$$

We define the lifetime, τ_{e}, via the relation $\sum_{k_x>0}\delta\dot{f}^{\mathrm{e}}_{k_x,\mathrm{R}} = -\frac{1}{\tau_{\mathrm{e}}}\sum_{k_x>0}\delta f^{\mathrm{e}}_{k_x\mathrm{R}}$. To extract the lifetime of the edge from Eq. (E11), we sum both sides of the equation over the momentum $k_x > 0$. The edge-to-edge scattering terms corresponding to the positive momenta, $k' > 0$ and $k > 0$ trivially cancel out. The edge-to-edge scattering terms that correspond to $k > 0$ and $k' < 0$, cancel out in the limit of small shift of the lead chemical potential, $\mu_{\mathrm{e}} \to 0$, $\delta f_{k_x\mathrm{R}} = \delta f_{-k_x\mathrm{R}}$. Here we used the particle-hole symmetry, $W^{\mathrm{ee},k'_x\mathrm{R}}_{k_x\mathrm{R}} = W^{\mathrm{ee},-k_x\mathrm{R}}_{-k'_x\mathrm{R}}$, and $f^{\mathrm{e},0}_{k_x\mathrm{R}} = \bar{f}^{\mathrm{e},0}_{-k_x\mathrm{R}}$. The expression for τ_{e} then contains only bulk-to-edge scattering terms, in agreement with Eq. (E9). The expression for τ_{e} reads

$$\tau_{\mathrm{e}} = \frac{\sum_{k_x>0}\delta f^{\mathrm{e}}_{k_x\mathrm{R}}}{\sum_{k_x>0}\sum_{\boldsymbol{k}'\alpha'}\big[W^{\mathrm{be},k_x\mathrm{R}}_{\boldsymbol{k}'\alpha'} f^{\mathrm{b},0}_{\boldsymbol{k}'\alpha'} + W^{\mathrm{eb},\boldsymbol{k}'\alpha'}_{k_x\mathrm{R}} \bar{f}^{\mathrm{b},0}_{\boldsymbol{k}'\alpha'}\big]\delta f^{\mathrm{e}}_{k_x\mathrm{R}}}. \tag{E12}$$

The values of τ_{e} obtained from numerically evaluating Eq. (E12) are plotted in the inset of Fig. 4(b). Our numerical results verify the prediction of the rate equations given in Eq. (E9).

3. Dependence of the chemical potential on the lead-system coupling

In this section, we study how the strength of the coupling to the lead [J in Eq. (12)] affects the position of the chemical potential of the edge, μ_{e}. Here we consider the part of the edge that is uniformly coupled to a lead [referring to Fig. 2(b), we discuss the edges along the x direction], hence the gradient term vanishes. We denote the shift of the lead chemical potential by μ_{res}, and below assume $\mu_{\mathrm{res}} > 0$. The continuity equations describing the electron and hole excitations at the right edge

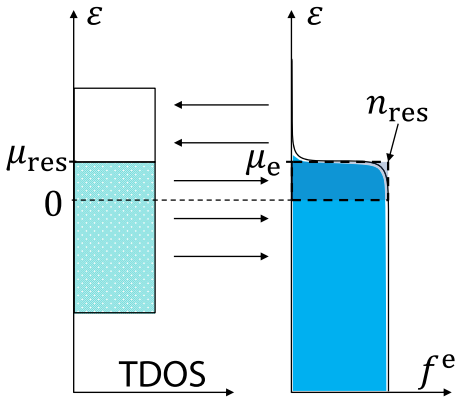

FIG. 8. Tunneling processes between the lead and the edge, when the chemical potential of the lead is shifted form the center of the band, at $\varepsilon = 0$. n_{res} is the density of edge states integrated over the energy interval $0 < \varepsilon < \mu_{res}$.

(Δn_e and Δh_e, respectively), at $y = L_y$, are then

$$\Delta\dot{n}_e = \gamma^{b\to e} n_b - \Lambda^{e\to b} n_b \Delta n_e - \gamma^{e\to e} \Delta n_e \Delta h_e - \bar{\mathcal{J}}_R(\Delta n_e - n_{res}), \tag{E13a}$$

$$\Delta\dot{h}_e = \gamma^{b\to e} n_b - \Lambda^{e\to b} n_b \Delta h_e - \gamma^{e\to e} \Delta n_e \Delta h_e - \bar{\mathcal{J}}_R \Delta h_e. \tag{E13b}$$

Here, $\bar{\mathcal{J}}_R$ is an average rate of edge-to-lead tunneling processes estimated as $\bar{\mathcal{J}}_R = \frac{1}{2k_R}\int_{-k_R}^{k_R} dk_x \mathcal{J}^0_{k_x R}$, and $n_{res} = \frac{\mu_{res}}{2\pi\hbar v_e}$ is the density of edge states integrated over the energy interval $0 < \varepsilon < \mu_{res}$, see Fig. 8. When μ_{res} is slightly shifted from $\varepsilon = 0$, the densities of electrons and holes are shifted by $\delta n_e = \Delta n_e - n_e$ and $\delta h_e = \Delta h_e - n_e$, respectively. To simplify the expressions for δn_e and δh_e we make the approximation that $\delta n_e = \delta h_e = 0$ for $\mu_{res} = 0$. The steady-state solution to Eqs. (E13a) and (E13b) (setting $\Delta\dot{n}_e = \Delta\dot{h}_e = 0$), to leading order in δn_e and δh_e, then reads

$$\delta n_e = \frac{\bar{\mathcal{J}}_R(\gamma^{e\to e} n_e + \Lambda^{e\to b} n_b + \bar{\mathcal{J}}_R)}{(\gamma^{e\to e} n_e + \Lambda^{e\to b} n_b + \bar{\mathcal{J}}_R)^2 - (\gamma^{e\to e} n_e)^2} n_{res}, \tag{E14a}$$

$$\delta h_e = -\frac{\bar{\mathcal{J}}_R \gamma^{e\to e} n_e}{(\gamma^{e\to e} n_e + \Lambda^{e\to b} n_b + \bar{\mathcal{J}}_R)^2 - (\gamma^{e\to e} n_e)^2} n_{res}. \tag{E14b}$$

We estimate the position of the effective chemical potential of the edge by $\mu_e \approx 2\pi\hbar v_e(\delta n_e - \delta h_e)$, then

$$\mu_e = \mu_{res} \frac{\bar{\mathcal{J}}_R}{\Lambda^{e\to b} n_b + \bar{\mathcal{J}}_R}. \tag{E15}$$

When $\bar{\mathcal{J}}_R \gg \Lambda^{e\to b} n_b$ the chemical potential of the edge and the reservoir are equal, see Fig. 4(a).

[1] S. Kohler, J. Lehmann, and P. Hänggi, Phys. Rep. **406**, 379 (2005).
[2] W. Yao, A. H. MacDonald, and Q. Niu, Phys. Rev. Lett. **99**, 047401 (2007).
[3] T. Oka and H. Aoki, Phys. Rev. B **79**, 081406 (2009).
[4] J.-i. Inoue and A. Tanaka, Phys. Rev. Lett. **105**, 017401 (2010).
[5] T. Kitagawa, E. Berg, M. Rudner, and E. Demler, Phys. Rev. B **82**, 235114 (2010).
[6] L. Jiang, T. Kitagawa, J. Alicea, A. R. Akhmerov, D. Pekker, G. Refael, J. I. Cirac, E. Demler, M. D. Lukin, and P. Zoller, Phys. Rev. Lett. **106**, 220402 (2011).
[7] N. H. Lindner, G. Refael, and V. Galitski, Nat. Phys. **7**, 490 (2011).
[8] T. Kitagawa, T. Oka, A. Brataas, L. Fu, and E. Demler, Phys. Rev. B **84**, 235108 (2011).
[9] Z. Gu, H. A. Fertig, D. P. Arovas, and A. Auerbach, Phys. Rev. Lett. **107**, 216601 (2011).
[10] N. H. Lindner, D. L. Bergman, G. Refael, and V. Galitski, Phys. Rev. B **87**, 235131 (2013).
[11] P. Delplace, Á. Gómez-León, and G. Platero, Phys. Rev. B **88**, 245422 (2013).
[12] Y. T. Katan and D. Podolsky, Phys. Rev. Lett. **110**, 016802 (2013).
[13] T. Iadecola, D. Campbell, C. Chamon, C.-Y. Hou, R. Jackiw, S.-Y. Pi, and S. V. Kusminskiy, Phys. Rev. Lett. **110**, 176603 (2013).
[14] A. Kundu, H. A. Fertig, and B. Seradjeh, Phys. Rev. Lett. **113**, 236803 (2014).
[15] G. Usaj, P. M. Perez-Piskunow, L. E. F. Foa Torres, and C. A. Balseiro, Phys. Rev. B **90**, 115423 (2014).
[16] T. A. Sedrakyan, V. M. Galitski, and A. Kamenev, Phys. Rev. Lett. **115**, 195301 (2015).
[17] M. Thakurathi, D. Loss, and J. Klinovaja, Phys. Rev. B **95**, 155407 (2017).
[18] V. Khemani, A. Lazarides, R. Moessner, and S. L. Sondhi, Phys. Rev. Lett. **116**, 250401 (2016).
[19] D. V. Else and C. Nayak, Phys. Rev. B **93**, 201103 (2016).
[20] A. C. Potter, T. Morimoto, and A. Vishwanath, Phys. Rev. X **6**, 041001 (2016).
[21] C. W. von Keyserlingk and S. L. Sondhi, Phys. Rev. B **93**, 245145 (2016).
[22] F. Harper and R. Roy, Phys. Rev. Lett. **118**, 115301 (2017).
[23] J. Klinovaja, P. Stano, and D. Loss, Phys. Rev. Lett. **116**, 176401 (2016).
[24] M. S. Rudner, N. H. Lindner, E. Berg, and M. Levin, Phys. Rev. X **3**, 031005 (2013).
[25] P. Titum, E. Berg, M. S. Rudner, G. Refael, and N. H. Lindner, Phys. Rev. X **6**, 021013 (2016).
[26] H. C. Po, L. Fidkowski, T. Morimoto, A. C. Potter, and A. Vishwanath, Phys. Rev. X **6**, 041070 (2016).
[27] D. V. Else, B. Bauer, and C. Nayak, Phys. Rev. Lett. **117**, 090402 (2016).

[28] J. Zhang, P. W. Hess, A. Kyprianidis, P. Becker, A. Lee, J. Smith, G. Pagano, I.-D. Potirniche, A. C. Potter, A. Vishwanath, N. Y. Yao, and C. Monroe, Nature (London) **543**, 217 (2017).

[29] S. Choi, J. Choi, R. Landig, G. Kucsko, H. Zhou, J. Isoya, F. Jelezko, S. Onoda, H. Sumiya, V. Khemani, C. von Keyserlingk, N. Y. Yao, E. Demler, and M. D. Lukin, Nature **543**, 221 (2017).

[30] Y. H. Wang, H. Steinberg, P. Jarillo-Herrero, and N. Gedik, Science **342**, 453 (2013).

[31] F. Mahmood, C.-K. Chan, Z. Alpichshev, D. Gardner, Y. Lee, P. A. Lee, and N. Gedik, Nat. Phys. **12**, 306 (2016).

[32] G. Jotzu, M. Messer, R. Desbuquois, M. Lebrat, T. Uehlinger, D. Greif, and T. Esslinger, Nature (London) **515**, 237 (2014).

[33] M. Aidelsburger, M. Lohse, C. Schweizer, M. Atala, J. T. Barreiro, S. Nascimbène, N. R. Cooper, I. Bloch, and N. Goldman, Nat. Phys. **11**, 162 (2015).

[34] M. Lohse, C. Schweizer, O. Zilberberg, M. Aidelsburger, and I. Bloch, Nat. Phys. **12**, 350 (2016).

[35] S. Nakajima, T. Tomita, S. Taie, T. Ichinose, H. Ozawa, L. Wang, M. Troyer, and Y. Takahashi, Nature Physics **12**, 296 (2016).

[36] N. Fläschner, D. Vogel, M. Tarnowski, B. S. Rem, D.-S. Lühmann, M. Heyl, J. C. Budich, L. Mathey, K. Sengstock, and C. Weitenberg, Nat. Phys. **14**, 265 (2018).

[37] M. C. Rechtsman, J. M. Zeuner, Y. Plotnik, Y. Lumer, D. Podolsky, F. Dreisow, S. Nolte, M. Segev, and A. Szameit, Nature (London) **496**, 196 (2013).

[38] L. J. Maczewsky, J. M. Zeuner, S. Nolte, and A. Szameit, Nat. Commun. **8**, 13756 (2017).

[39] H. Dehghani, T. Oka, and A. Mitra, Phys. Rev. B **90**, 195429 (2014).

[40] H. Dehghani, T. Oka, and A. Mitra, Phys. Rev. B **91**, 155422 (2015).

[41] T. Iadecola and C. Chamon, Phys. Rev. B **91**, 184301 (2015).

[42] T. Iadecola, T. Neupert, and C. Chamon, Phys. Rev. B **91**, 235133 (2015).

[43] K. I. Seetharam, C.-E. Bardyn, N. H. Lindner, M. S. Rudner, and G. Refael, Phys. Rev. X **5**, 041050 (2015).

[44] D. E. Liu, A. Levchenko, and R. M. Lutchyn, Phys. Rev. B **95**, 115303 (2017).

[45] M. Genske and A. Rosch, Phys. Rev. A **92**, 062108 (2015).

[46] X. Dang, J. D. Burton, A. Kalitsov, J. P. Velev, and E. Y. Tsymbal, Phys. Rev. B **90**, 155307 (2014).

[47] B. A. Bernevig, T. L. Hughes, and S.-C. Zhang, Science (N.Y.) **314**, 1757 (2006).

[48] O. Zitouni, K. Boujdaria, and H. Bouchriha, Semicond. Sci. Technol. **20**, 908 (2005).

[49] H. Sambe, Phys. Rev. A **7**, 2203 (1973).

[50] J. H. Shirley, Phys. Rev. **138**, B979 (1965).

[51] V. M. Galitskii, S. P. Goreslavskii, and V. F. Elesin, Zh. Eksp. Teor. Fiz. **57**, 207 (1969) [Sov. Phys.–JETP **30**, 117 (1970)].

[52] D. E. Liu, Phys. Rev. B **91**, 144301 (2015).

[53] T. Shirai, T. Mori, and S. Miyashita, Phys. Rev. E **91**, 030101 (2015).

[54] T. Shirai, J. Thingna, T. Mori, S. Denisov, P. Hänggi, and S. Miyashita, New J. Phys. **18**, 053008 (2016).

[55] K. Iwahori and N. Kawakami, Phys. Rev. B **94**, 184304 (2016).

[56] M. I. Dykman, M. Marthaler, and V. Peano, Phys. Rev. A **83**, 052115 (2011).

[57] F. R. Ong, M. Boissonneault, F. Mallet, A. C. Doherty, A. Blais, D. Vion, D. Esteve, and P. Bertet, Phys. Rev. Lett. **110**, 047001 (2013).

[58] G. Conibeer, C.-W. Jiang, D. König, S. Shrestha, T. Walsh, and M. Green, Thin Solid Films **516**, 6968 (2008).

[59] S. K. Shrestha, P. Aliberti, and G. J. Conibeer, Solar Energy Mater. Solar Cells **94**, 1546 (2010).

[60] D. J. Farrell, Y. Takeda, K. Nishikawa, T. Nagashima, T. Motohiro, and N. J. Ekins-Daukes, Appl. Phys. Lett. **99**, 111102 (2011).

[61] C. Schmuttenmaer, C. Cameron Miller, J. Herman, J. Cao, D. Mantell, Y. Gao, and R. Miller, Chem. Phys. **205**, 91 (1996); A. Tanaka, N. J. Watkins, and Y. Gao, Phys. Rev. B **67**, 113315 (2003); K. Wang, J. Wang, J. Fan, M. Lotya, A. O'Neill, D. Fox, Y. Feng, X. Zhang, B. Jiang, Q. Zhao, H. Zhang, J. N. Coleman, L. Zhang, and W. J. Blau, ACS Nano **7**, 9260 (2013); D. Niesner, S. Otto, T. Fauster, E. Chulkov, S. Eremeev, O. Tereshchenko, and K. Kokh, J. Electron Spectrosc. Relat. Phenom. **195**, 258 (2014).

[62] M. Claassen, C. Jia, B. Moritz, and T. P. Devereaux, Nat. Commun. **7**, 13074 (2016).

[63] A. Nafidi, in *Optoelectronics - Advanced Materials and Devices* (InTech, Croatia, 2013); S. Safa, A. Asgari, and L. Faraone, J. Appl. Phys. **114**, 053712 (2013); H. Schmidt, F. Giustiniano, and G. Eda, Chem. Soc. Rev. **44**, 7715 (2015); S. Xu, Z. Wu, H. Lu, Y. Han, G. Long, X. Chen, T. Han, W. Ye, Y. Wu, J. Lin, J. Shen, Y. Cai, Y. He, F. Zhang, R. Lortz, C. Cheng, and N. Wang, 2D Mater. **3**, 021007 (2016).

[64] N. Nagaosa, J. Sinova, S. Onoda, A. H. MacDonald, and N. P. Ong, Rev. Mod. Phys. **82**, 1539 (2010).

[65] J. P. Dahlhaus, B. M. Fregoso, and J. E. Moore, Phys. Rev. Lett. **114**, 246802 (2015).

[66] K. C. Nowack, E. M. Spanton, M. Baenninger, M. König, J. R. Kirtley, B. Kalisky, C. Ames, P. Leubner, C. Brüne, H. Buhmann, L. W. Molenkamp, D. Goldhaber-Gordon, and K. A. Moler, Nat. Mater. **12**, 787 (2013).

[67] E. M. Spanton, K. C. Nowack, L. Du, G. Sullivan, R.-R. Du, and K. A. Moler, Phys. Rev. Lett. **113**, 026804 (2014).

[68] L.-J. Yin, H. Jiang, J.-B. Qiao, and L. He, Nat. Commun. **7**, 11760 (2016).

[69] Y. Ji, Y. Chung, D. Sprinzak, M. Heiblum, D. Mahalu, and H. Shtrikman, Nature **422**, 415 (2003).

[70] N. Tsuji, T. Oka, and H. Aoki, Phys. Rev. B **78**, 235124 (2008).

[71] T. Bilitewski and N. R. Cooper, Phys. Rev. A **91**, 063611 (2015).

[72] M. Bukov, M. Heyl, D. A. Huse, and A. Polkovnikov, Phys. Rev. B **93**, 155132 (2016).

[73] J. Rammer, *Quantum Field Theory of Non-equilibrium States* (Cambridge University Press, New York, 2007).

[74] A. Kamenev, *Field Theory of Non-equilibrium Systems* (Cambridge University Press, Cambridge, UK, 2011).

[75] A. I. Larkin and Y. N. Ovchinnikov, in *Nonequilibrium Superconductivity*, edited by D. N. Langenberg and A. I. Larkin (Elsevier Science, Amsterdam, 1986), Chap. 11.

[76] M. J. Moelter, J. Evans, G. Elliott, and M. Jackson, Am. J. Phys. **66**, 668 (1998).

[77] D. W. Hone, R. Ketzmerick, and W. Kohn, Phys. Rev. E **79**, 051129 (2009).